University of Tartu
Faculty of Science and Technology
Institute of Chemistry

Umber Sajjad

OXYGEN ELECTROREDUCTION ON LIGNIN-DERIVED NON-PRECIOUS METAL CATALYSTS

Master's Thesis (30 ECTS)
Curriculum: Materials Science and Technology

Supervisors:
Kaido Tammeveski, PhD
Ave Sarapuu, PhD

Tartu 2023

Abstract

Oxygen electroreduction on lignin-derived non-precious metal catalysts

In this study, doped nanocarbon electrocatalysts for electrochemical oxygen reduction reaction were prepared from lignin as a carbon source. The synthesis was carried out by high-temperature pyrolysis in the presence of cobalt and iron salts, dicyandiamide as nitrogen source and magnesium acetate as a precursor for MgO template to increase the specific surface area of the catalysts. The structure and composition of the catalysts were characterised by several physicochemical analysis methods. In rotating disk electrode tests under alkaline conditions, the electrocatalysts showed high activity for the oxygen reduction reaction, which depended on iron content in the catalyst, and high stability in potential cycling. In anion-exchange membrane fuel cell test, the bimetallic catalyst showed higher performance as compared to iron-containing material, producing a peak power density of 675 mW cm^{-2}.

Keywords: oxygen reduction, electrocatalysis, non-precious metal catalyst, anion exchange membrane fuel cell, lignin.

CERCS: P401 Electrochemistry

Lühikokkuvõte

Hapniku elektroredutseerumine ligniinipõhistel mitteväärismetallkatalüsaatoritel

Töös valmistati dopeeritud nanostruktuursed süsinikkatalüsaatorid elektrokeemilise hapniku redutseerumisreaktsiooni jaoks, kasutades süsinikuallikana ligniini. Katalüsaatormaterjalide süntees viidi läbi kõrgtemperatuursel pürolüüsil koobalti- ja rauasoolade ning lämmastikuallikana ditsüaandiamiidi juuresolekul, kasutades magneesiumatsetaati MgO matriitsi lähteainena, et saada suurema eripinnaga katalüsaatoreid. Katalüsaatorite struktuuri ja koostist iseloomustati mitmete füsikokeemiliste meetoditega. Pöörleva ketaselektroodi testides aluselises lahuses näitasid elektrokatalüsaatorid kõrget aktiivsust, mis sõltus katalüsaatori rauasisaldusest, ja ka head stabiilsust potentsiaali tsükleerimisel. Anioonivahetusmembraaniga kütuseelemendi testides oli bimetalsel elektrokatalüsaatoril kõrgem jõudlus võrreldes rauda sisaldava materjaliga, saavutades maksimaalse võimsustiheduse 675 mW cm^{-2}.

Märksõnad: hapniku redutseerumine, elektrokatalüüs, mitteväärismetallkatalüsaator, anioonvahetusmembraaniga kütuseelement, ligniin.

CERCS: P401 Elektrokeemia

Contents

Abbreviations

AEM	anion exchange membrane
AEMFC	anion exchange membrane fuel cell
BET	Brunauer-Emmett-Teller
$C_{O_2}^b$	concentration of oxygen in the bulk solution
DCDA	dicyandiamide
DFT	density functional theory
D_{O_2}	diffusion coefficient of oxygen
E	electrode potential
E_0	standard potential
$E_{1/2}$	half-wave potential
EDX	energy-dispersive X-ray spectroscopy
E_{onset}	onset potential
GC	glassy carbon
GDE	gas diffusion electrode
GDL	gas diffusion layer
I	current
I_{d}	diffusion-limited current
I_{k}	kinetic current
j	current density
j_{d}	diffusion-limited current density
j_{k}	kinetic current density
k	electrochemical rate constant for O_2 reduction
MA	mass activity
M-N-C	metal-nitrogen-carbon
M-N_x	metal coordinated to nitrogen
n	number of electrons transferred per O_2 molecule
OMC	ordered mesoporous carbon
ORR	oxygen reduction reaction
PEMFC	proton exchange membrane fuel cell
PGM	platinum-group metals
P_{max}	peak power density
RDE	rotating disc electrode

rpm	revolutions per minute
SCE	saturated calomel electrode
SEM	scanning electron microscopy
SHE	standard hydrogen electrode
SSA	specific surface area
STEM	scanning transmission electron microscopy
V_{micro}	micropore volume
V_{tot}	total pore volume
XPS	X-ray photoelectron spectroscopy
XRD	X-ray diffraction
ν	kinematic viscosity of the solution
ω	rotation rate of the electrode

Introduction

The energy crisis is on the rise, with fossil fuels such as oil, natural gas, and coal providing 80% of all energy consumed globally. This has led to an increase in energy consumption and depletion of fossil fuel reserves, threatening energy and economic security worldwide and releasing greenhouse gases and other pollutants [1].

Hydrogen is viewed as playing a crucial part in the energy system for a clean and sustainable future. Due to its great gravimetric energy density, lack of toxicity, and lack of environmental impact, hydrogen is the ideal energy carrier. While non-renewable sources can be used to generate hydrogen, its production is moving more and more in the direction of using renewable methods, such as using wind or solar energy to electrolyse water [2].

Fuel cells are promising electrochemical energy conversion devices, where hydrogen is transformed cleanly into electrical energy and only water is produced as a by-product [3]. The slow oxygen reduction reaction (ORR), which occurs at the fuel cell cathode, is one of the main problems to solve in the fuel cell technology. The O_2 molecule needs a suitable electrocatalyst to be split at a significant rate because of the strong oxygen-oxygen double bond. Platinum-based catalysts have been employed on the cathode of practically all commercially available fuel cell systems up to this point, but it has become clear that these materials cannot meet the long-term activity and stability goals while maintaining sufficiently low costs [4]. A huge amount of research has been conducted in search of replacing Pt in fuel cells with cheaper, more durable, highly performing, and earth-abundant catalysts [5].

The quest to find an alternative to the platinum catalyst has consistently gained speed ever since Jasinski published his research on a non-platinum fuel cell catalyst in 1964 [6]. Non-precious metal catalysts have been developed for the electrochemical oxygen reduction reaction. Heteroatom-doped carbon nanomaterials and transition metal–nitrogen–carbon (M–N–C) catalysts are especially advantageous in an alkaline environment [7].

The goal of this master's thesis was to develop platinum-free electrocatalysts for the ORR that could be used on the cathode of an anion exchange membrane fuel cell. In catalyst preparation, lignin was used as a sustainable organic precursor. Through high-temperature pyrolysis in the presence of dicyandiamide as nitrogen precursor and transition metal salts, nanostructured carbon-based materials doped with nitrogen and transition metals (iron and cobalt) were prepared. To increase the specific surface area of catalysts, magnesium acetate was used as a template precursor. In half-cell tests using the rotating disc electrode method, it was determined how the structure and composition of the catalysts affect their ORR activity.

1. Literature overview

1.1. Electrochemical oxygen reduction reaction

One of the most essential electrochemical processes is the oxygen reduction reaction (ORR). It serves as the foundation for life through biological respiration and supplying energy via fuel cells. The ORR in acidic aqueous solutions can proceed through a 4-electron or 2-electron route [8]:

$$O_2 + 4H^+ + 4e^- \rightarrow 2H_2O \quad (1)$$

$$O_2 + 2H^+ + 2e^- \rightarrow H_2O_2 \quad (2)$$

The H_2O_2 formed can be further reduced:

$$H_2O_2 + 2H^+ + 2e^- \rightarrow 2H_2O \quad (3)$$

In alkaline media the ORR can also proceed via two pathways. The 4-electron pathway is [9]:

$$O_2 + 2H_2O + 4e^- \rightarrow 4OH^- \quad (4)$$

The 2-electron pathway:

$$O_2 + 2H_2O + 2e^- \rightarrow HO_2^- + OH^- \quad (5)$$

Further reduction of hydroperoxide anion:

$$2HO_2^- + H_2O + 2e^- \rightarrow 3OH^- \quad (6)$$

The four-electron pathway is preferred, because it is more energy efficient. The ORR mechanism involves the adsorption of oxygen on the electrode surface and subsequent reduction through dissociative or associative pathways. The choice of pathway depends on factors such as oxygen coverage and electrode material. The binding energy of intermediate oxygen species on the electrode surface affects the electrocatalytic activity, with an optimal catalyst having a moderate binding. Platinum exhibits one of the most optimal binding energies compared to the other metals [9].

1.2. Non-precious metal catalysts for ORR

Developing highly active, stable, and cost-effective cathode catalysts for ORR is important to promote the widespread applicability of fuel cells. Platinum group metal (PGM)-free nanostructured carbon-based catalysts containing heteroatoms or metal–nitrogen–carbon (M–N–C) sites are promising candidates due to their low cost and high electrocatalytic activity towards the ORR [10].

Several carbon nanomaterials like carbon nanotubes [11], graphene [12] and carbide-derived carbon (CDC) [13] have undergone substantial research as electrocatalysts for ORR in alkaline solutions. Due to the recent advancements in the design of materials for alkaline fuel cells, interest in ORR on carbon-based materials is growing. To increase the ORR activity of carbon

materials, doping with various heteroatoms is widely employed. Nitrogen [14], sulphur [15][16], phosphorus [17], boron[18], fluorine [19] and iodine [20] have been used for doping carbon materials. Heteroatom doping can adjust adsorbability, spin and charge distribution, and hydrophilicity of carbon materials [21]. Adding electron-accepting nitrogen atoms to the conjugated carbon plane gives nearby carbon atoms a rather high positive charge density [14]. Oxygen can more readily be adsorbed and reduced on these sites [8].

The nitrogen atoms in carbon matrix can exist in different bonding configurations, from which quaternary N, pyridinic N, and pyrrolic N are most common [22] (Figure 1). Pyridinic nitrogen is the most reported type of N species responsible for the high ORR activity of N-doped carbon materials. For example, Rao et al. [23] and Miao et al. [24] reported an increased catalytic activity of N-doped carbon nanotubes due to the increase in the atomic percentage of pyridinic N species.

Heteroatom-doped carbon nanomaterials are active ORR catalysts in alkaline environment, but by adding transition metals (Fe, Co, Mn, etc.) to the catalyst composition the M–N–C catalysts can be obtained, which have demonstrated significantly improved electrocatalytic activity and stability in both acidic and alkaline electrolytes [25]. These materials have shown the ORR performance that is equivalent to or occasionally even higher than that of Pt/C catalysts [26]. Such catalysts contain atomically dispersed transition metal atoms coordinated to nitrogen species ($M\text{-}N_x$) as main active centres that show high activity in both acidic and alkaline solution [27]. The exact role of all active sites is still a matter of controversy, in addition, factors like the carbon structure, nearby functional groups, and electrolyte pH can influence the electrocatalytic activity of these sites [26]. It has been shown that the key activity descriptor controlling ORR electrocatalysis on $Fe\text{-}N_x$ active sites is the carbon support's capacity to donate or remove electrons [28].

Iron and cobalt have received the greatest attention as transition metals in M-N-C type catalysts [29-32]. Although both iron- and cobalt-based catalyst show high ORR activity, the cobalt-based catalysts show higher production of hydrogen peroxide. This is explained by the fact that on Co-N-C catalyst materials, peroxide desorption may occur more quickly [9].

Cobalt and iron combined in a single catalyst material have demonstrated favourable ORR performance, even outperforming the activity of single-metal counterpart [31]. The synergistic interactions between the $Fe\text{-}N_4$ and $Co\text{-}N_4$ active centres is thought to be the cause of increased ORR activity. According to DFT calculations, Fe and Co display higher ORR activity in nearby $Fe\text{-}N_4$ and $Co\text{-}N_4$ active sites than in monometallic $Fe\text{-}N_4$ and $Co\text{-}N_4$ sites located separately [32].

The porous structure of the catalysts also affects their ORR electrocatalytic activity. Micropores (pore diameter <2 nm), mesopores (pore diameter 2-50 nm), and macropores (pore diameter >50 nm) are essential in Fe-N-C electrocatalysts because they increase the active surface that is accessible to electrolytes and make it easier to transfer products as well as reactants. This results in a greater utilization of active sites [33]. Microporous structure with high surface area is beneficial for the design of atomically dispersed M-N-C catalysts [34].

In order to prepare the catalyst materials with high density of M-N-C sites, it is important to inhibit the free movement of metal atoms and prevent the formation of nanoparticles. N-containing organic compounds can provide N atoms with isolated electron pairs and form stable M–N bonds. Metal-organic frameworks with metal nodes and N-containing ligands can also provide N coordination sites for transition metal atoms [35].

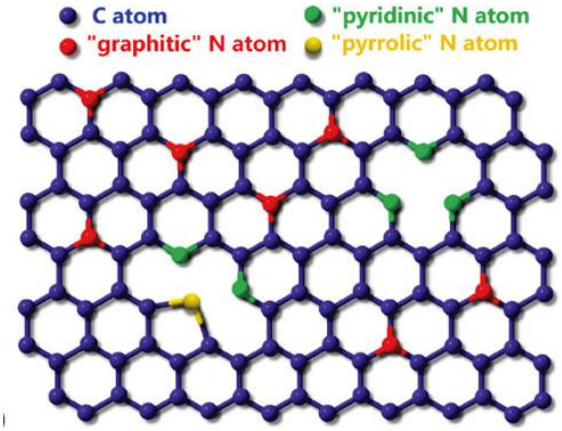

Figure 1: Different types of nitrogen moieties in nitrogen-doped carbon catalyst [35].

1.3. Preparation of carbon-based non-precious metal catalysts from biomass

1.3.1. Sources of biomass

Biomass, which is abundant and renewable, can be utilized to create a variety of carbon materials with distinct characteristics. The nature, structure, and chemical makeup of the biomass source, among other factors, influence the properties of these materials, creating a complex field of study for biomass-derived carbon chemistry. These materials have multiple applications, including energy storage, sensing, environmental remediation, and electrocatalysis [15][36][37].

The three primary categories of biomass resources are plant biomass (e.g., agricultural residues, seaweed, and algae), animal and human waste biomass (e.g., blood, bone, and tannery waste), and microorganisms like fungi and bacteria. Animal-derived proteins, chitin, and keratin are

utilized for carbon material synthesis, with proteins being suitable for N-doped carbon-based electrocatalysts and chitosan aiding dopant incorporation. Fungi and bacteria are used to synthesize heteroatom-doped carbon materials, creating defects and active sites that are useful for various catalyst applications [15].

Plant-based biomass consisting mainly of cellulose, hemicellulose and lignin is most widely used for preparation of carbon materials. Cellulose is a glucose-based polysaccharide that forms micro-fibrils in plants and bacteria. Hemicellulose, the second most abundant biomass resource in nature after cellulose, is a polymer composed of sugar-based units, including five, six, and seven-membered carbon heterocycles linked together through hydrogen bonds [15]. Lignin is an abundant component in plant biomass and the most prevalent aromatic polymer found in nature [38]. The phenolic components that make up lignin, such as *p*-coumaryl alcohol, sinapyl alcohol, and coniferyl alcohol, are combined to yield a complicated amorphous polymer (Figure 2). It has a number of links, the most prevalent of which is β-o-4. Determining the precise structure of various lignins is difficult due to the versatile nature of polymerization [39]. Thanks to its high carbon content, lignin has been suggested as a precursor for the manufacture of carbon compounds such as activated carbons that are used in electrochemical processes [38].

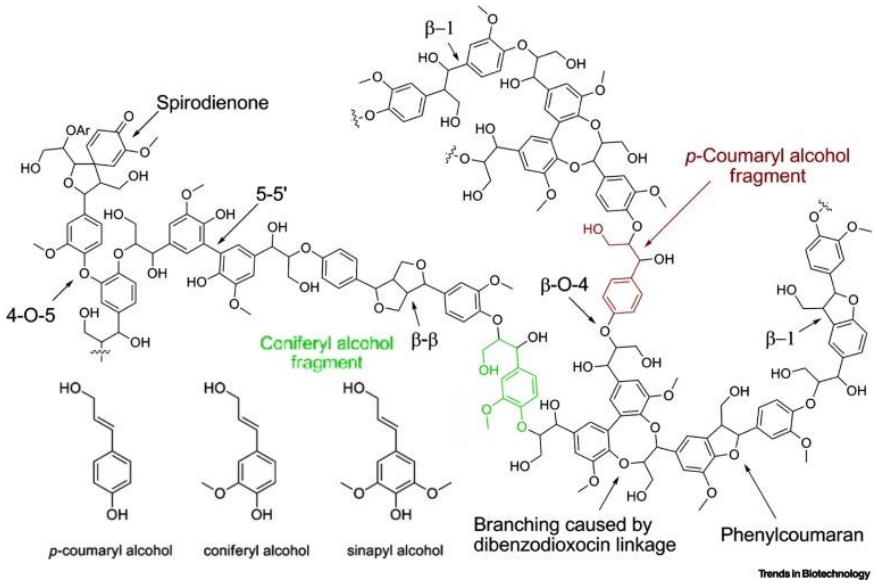

Figure 2: Proposed chemical structure of lignin [39].

1.3.2. Preparation methods of heteroatom-doped carbon materials

The methods of preparation of heteroatom-doped carbon materials from biomass can be divided into two categories: (i) intrinsic doping, where the heteroatoms originate from the components of the biomass precursor, and (ii) extrinsic doping, where the heteroatoms have been consciously added during the synthesis of the carbonaceous material [15].

Pyrolysis, a thermal degradation process, is widely employed for creating porous carbon materials derived from natural biomass. It is a versatile technique that can be utilized for a range of biomass feedstocks while also allowing for adjustable operating parameters. The procedure entails heating dry biomass at high temperatures in an inert atmosphere or low-oxygen environment. Pyrolysis is a process that involves various chemical reactions such as dehydration, condensation, depolymerisation, and fragmentation of biomass, which ultimately result in the transformation of biomass into porous carbons. The pyrolysis procedure can be divided into three discrete phases, each involving distinct chemical reactions and the release of oxygen atoms, primarily in the form of carbon monoxide and carbon dioxide. Pyrolysis yields various end products, including gaseous compounds, bio-oil, and biochar. The relative quantities of said products are contingent upon the specific parameters of the pyrolysis process. The most efficient technique for producing biochar with a high yield is slow pyrolysis, which is also referred to as carbonization. The fast pyrolysis and gasification methods predominantly produce bio-oil and gases, respectively, while the biochar yield is comparatively lower [40]. Carbon produced from pure biomass usually possesses low specific surface area, thus being useless as a catalyst material. Therefore, it is necessary to activate the biomass, which may be done by adjusting the porosity, surface area, and binding capacity [41].

The term "**physical activation**" refers to a regulated process of material gasification, which involves the use of an oxidizing gas, such as oxygen, water vapour, and carbon dioxide, at a specific temperature. This process is carried out subsequent to an initial pyrolysis phase under an inert gas [15]. Physical activation affords to produce activated porous carbons with moderate specific surface areas (SSA) <1000 $m^2 g^{-1}$ and narrow micropores [40].

Chemical activation, on the other hand, refers to the chemical assault by molten reagents like $ZnCl_2$, KOH, or NaOH. Chemical activation is frequently carried out by impregnating the biomass precursor with the reagent or by physically mixing them together. The next step is a heat treatment. After cooling, the material is washed with water to remove any remaining chemical agents, filtered, and dried [15]. Chemical activation can lead to highly porous carbons (SSA ~ 3000 $m^2 g^{-1}$) [40].

The self-activation process, which produces activated carbon without extra activating chemicals, is economically and environmentally sustainable. The air in the enclosed reactor vessel and oxygen adsorbed on the raw biomass material both act as activating agents in self-activation. The gas generated during the pyrolysis of the biomass precursors is used to activate the carbon during the physical activation process. In addition, the inorganic compounds present in the biomass can help to activate carbon during the chemical self-activation process [41].

Mechanosynthesis is an alternative method for preparing carbon-based materials, which uses mechanical forces such as ball milling to convert biomass into carbon materials. Recent studies have shown that it can achieve high yield without using toxic solvents, but an additional pyrolysis step may be recommended for certain applications [15].

Hydrothermal carbonization is an alternative method for synthesizing biomass-derived carbons. It involves heating biomass at mild temperatures (175–300 °C) in pure water at autogenous high pressure, which facilitates the hydrolysis and cleavage of the chemical structure of biomass. Other simultaneous reactions occur during the process, such as dehydration, decarboxylation, aromatization, and condensation, which affect the structural rearrangement of biomass. Hydro-char is an insoluble product composed of condensed aromatic structures with many oxygen-containing functional groups. The initial structure and composition of biomass precursors greatly influence the shape and surface properties of hydro-char. The addition of a catalyst can improve the reaction rate and affect the morphology and structure of the obtained hydro char [40].

Template-based methods are often used to prepare carbon materials with desired porous structure. In the hard template approach temperature-resistant nanoparticles or other nanostructures, such as silicas, zeolites, or metal oxides are included to the pyrolysis precursors and dissolved after the pyrolysis, yielding the pores with the size and shape of the template [41]. Silica-based templates are most commonly used, but require harsh chemicals for their removal, such as HF or concentrated NaOH [9].

Inorganic particles that can be more easily removed, like MgO, $CaCO_3$, and ZnO, are viable substitutes for silica-based templates used to produce carbon materials. Inagaki et al. [42] recommended procedure, in which a carbon precursor is pyrolyzed along with MgO or thermally unstable magnesium compounds like acetate, citrate, or gluconate. These precursors break down during heat treatment to create MgO nanoparticles, which can then be dissolved using dilute HCl. The porous structure of the final carbon material will vary depending on the carbon nanomaterial, MgO precursors, and the mass ratio of MgO to the precursor [25]. MgO template-assisted method has been used for synthesizing mesoporous nitrogen and transition

metal co-doped carbon catalysts from alkylresorcinols as carbon source, dicyandiamide, Fe and Co salts as nitrogen and transition metal sources [43].

Soft-templating involves the cooperative self-assembly of amphiphilic molecules and carbon precursors to form organic–organic hydrogen-bonded mesophases [8]. The main advantage of this method is that template decomposes during the pyrolysis, so there is no need for additional template removal step. Control of polymerization rate and pH is important for successful soft template synthesis of ordered mesoporous carbons (OMCs), as it affects the reaction mechanism and resulting product. OMCs can be synthesized under both acidic and basic conditions, with the pore size being tuned by changing the carbonization temperature, carbon precursors/template proportion, and surfactants [40].

1.4. Oxygen reduction on lignin-derived non-precious metal catalysts

There are number of lignin-based catalyst that have been reported for their good electrocatalytic activity for ORR. For example, N and S co-doped carbon nanosheets prepared by carbonization of ammoniated sodium lignosulfonate showed moderate ORR activity and good stability [44]. N, S-co-doped graphitic carbon sheets were obtained by pyrolysis of bagasse lignin in the presence of urea and melamine. The mass ratio of precursors and the pyrolysis temperature was optimised and the most active catalyst showed the ORR activity comparable to that of Pt/C in alkaline solution. In acidic solution, however, the electro catalytic activity was moderate [45]. N, S-co-doped flower-like porous carbon catalysts were synthesised from lignosulfonate and melamine in the presence of flower-like magnesium oxide (MgO) templates and $ZnCl_2$ as an activator. The materials showed high ORR activity and long-term durability in alkaline solution [46].

Activated char made from waste lignin via pyrolysis in the presence of $KHCO_3$ was used as a support for the production of transition metal-nitrogen-carbon electrocatalysts. Iron and/or manganese phthalocyanines were used as metal and nitrogen source for doping the carbon in high-temperature pyrolysis. The electrocatalysts showed good oxygen reduction reaction activity in both acidic and alkaline environments, with the bimetallic L_FeMn electrocatalyst exhibiting lowest peroxide yield in alkaline media. Peak power densities of 261 mW cm^{-2} and 72 mW cm^{-2} were achieved by with the LFeMn electrocatalyst in anion exchange membrane fuel cells and proton exchange membrane fuel cells tests, respectively [47].

N-doped carbon nanosheets were derived by pyrolysis of ball-milled mixtures of alkali lignin, NH_4Cl, and $ZnCl_2$. The catalyst exhibited good ORR performances, stability, methanol tolerance, and rechargeable zinc-air battery performance [48].

Fe- and N-doped carbon nanotubes were synthesized from lignin derived by enzymatic hydrolysis. For this, a Fe–lignin complex was prepared by hydrothermal treatment of lignin with Fe salt and urea, mixed with dicyandiamide and pyrolyzed. The metal content and pyrolysis temperature were varied, and the most active catalyst showed high ORR activity in alkaline solution and ZAB performance similar to those of Pt/C [49].

Cobalt- and/or nickel-containing N-doped catalysts were obtained by hydrothermal treatment of aminated alkali lignin and studied as electrocatalysts for ORR and OER reactions. The bimetallic material exhibited the best bifunctional performance in alkaline solution [50].

1.5. Low-temperature fuel cells

Fuel cell technology is a solution to meet future energy demands due to its low greenhouse gas emissions, quiet operation, and high efficiency in converting chemical energy into electricity. There are six primary categories of fuel cells: proton exchange membrane fuel cells (PEMFC), alkaline fuel cells (AFC), phosphoric acid fuel cells (PAFC), molten carbonate fuel cells (MCFC), solid oxide fuel cells (SOFC), and microbial fuel cells (MFC). PEMFC, AFC, PAFC, and MFC operate at low temperatures between 50 and 200 °C, whereas MCFC and SOFC work at high temperatures between 650 and 1000 °C [51].

A fuel cell consists of a non-conductive electrolyte material sandwiched between two electrodes, where the fuel and oxidant are fed to the anode and cathode sides (Figure 3) [52].

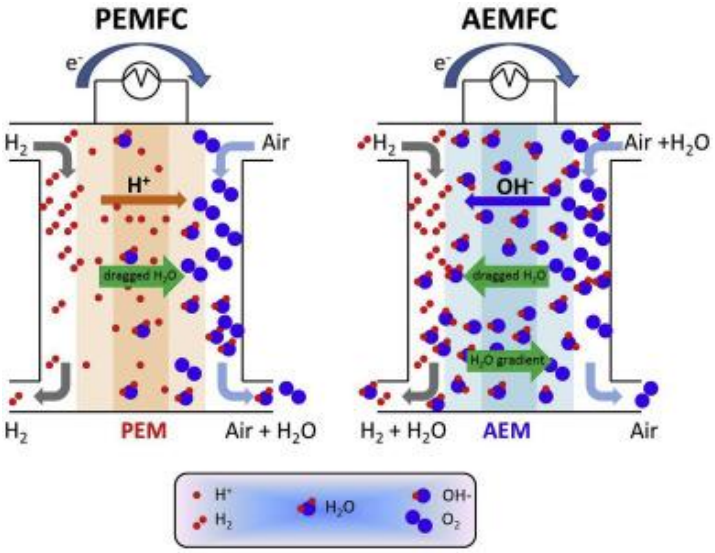

Figure 3: Schematic of PEMFC and AEMFC. Adopted from [52].

In PEMFC, hydrogen passes through an anode feeding channels and is oxidized into protons and electrons. Oxygen is fed to the cathode and is reduced to water [53]. The PEMFCs are already commercially available and used, for instance, in the fuel cell vehicles. However, this technology is still rather expensive, as it needs costly Pt-based catalysts [53].

Anion exchange membrane fuel cells (AEMFCs) have been increasingly studied in last decade due to their ability to use non-precious metal catalysts, reducing cost per kilowatt of power [54]. The AEMFC consists of an anode, a cathode, and an anion exchange membrane (AEM) sandwiched between them to form a membrane electrode assembly (MEA), which is supported by gas diffusion layers (GDLs). The AEM should have the ability to transport OH^- ions while preventing fuel crossover and blocking the transport of electrons [55].

To achieve high performance of AEMFCs, the most important issues to be addressed are: (1) the utilization of stable, high conductivity, and high water transport membranes; (2) the regulation of water content and balance in functional cells; (3) the development and optimization of electrodes; and (4) the mitigation of the adverse impacts of CO_2 [56].

The relatively low conductivities of the AEMs were initially the main source of concern in AEMFC technology [52]. By now, increased stability, high ionic conductivities, and improved water transport properties of advanced AEMs, especially radiation-grafted AEMs (RG-AEMs), have showed promise for AEMFC applications. To improve the functionality of RG-AEMs, researchers have optimised the graft polymerization conditions [57].

Improper water management, carbonation, and degradation of components can lead to AEMFC performance losses [58]. A problem in their design is the swelling of AEMs brought on by water. High anionic conductivity requires a high number of functionalized cationic groups, yet this can result in greater swelling and decreased membrane mechanical strength. Finding a compromise between achieving ideal anionic conductivity and preserving appropriate mechanical characteristics in AEMs is hence the key problem [59]. Performance degradation is caused by the chemical degradation of ionomers and AEMs in highly alkaline environments, which reduces membrane conductivity and increases cell resistance, resulting in reduced durability [60].

US Department of Energy (DOE) has proposed milestones for the next ten years for the performance and durability of AEMFC MEAs. These milestones address the most challenging aspects of AEMFC MEAs, such as raising initial performance and durability under realistic operating conditions while decreasing PGM loading and improving CO_2 tolerance. By 2030, the target is to demonstrate the initial performance of 600 mW cm^{-2} under H_2/air in PGM-free MEA with A ≥25 cm^2 MEA [61].

2. Experimental

2.1. Preparation of catalysts

The electrocatalysts were prepared using lignin (finely ground Lignova™ Crude, Fibenol, Estonia) as the carbon precursor, dicyandiamide (DCDA, Sigma-Aldrich) and $Fe(NO_3)_3 \cdot 9H_2O$ (97%, Sigma-Aldrich) and $Co(NO_3)_2 \cdot 6H_2O$ (98%, Sigma-Aldrich) as the nitrogen and transition metal precursors. Certain amounts of Fe nitrate were dissolved in the mixture of 30 ml of Milli-Q water (Millipore Inc.) and 30 ml of 2-propanol, after which 0.2 g lignin, 2 g DCDA and 0.1 g of $Mg(CH_3COO)_2 \cdot 4H_2O$ (98% Alfa Aesar) were added. The amount of the iron salt used was chosen so that the Fe content in it would be 7.5 mg, 15 mg, 30 mg and 60 mg for preparation of catalyst materials denoted as Fe1/4NC(Mg), Fe1/2NC(Mg), FeNC(Mg) and Fe2NC(Mg), respectively. The mixture was dried at 60 °C overnight, the dry powder was ground in a mortar and pyrolysed for two hours at 800 °C, ramping up at a rate of 10 °C min^{-1}. To dissolve the MgO template after pyrolysis, the products were mixed in 1 M HCl (Sigma-Aldrich) at room temperature for 2 h. The resulting carbon materials underwent filtering, washing with Milli-Q water, drying and a second pyrolysis at 800 °C for 2 h. For comparison, a bimetallic catalyst containing Fe and Co (FeCoNC(Mg)) was prepared following the same procedure and using 15 mg of Co and 15 mg of Fe as respective transition metal salts. In addition, a metal-free catalyst (NC(Mg)) was prepared with the same procedure but without adding any metal salts, and an iron-containing catalyst was prepared without adding Mg acetate as template precursor and employing 30 mg of Fe in the synthesis, denoted as FeNC. In the preparation of this material, no acid treatment and 2nd pyrolysis was used.

2.2. Physicochemical characterization methods

The scanning electron microscopy (SEM) and scanning transmission electron microscopy (STEM) measurements and the energy-dispersive X-ray spectroscopy (EDX) analysis were performed by Dr. Jekaterina Kozlova in the Institute of Physics, University of Tartu. The N_2 physisorption analysis was conducted by Dr. Maike Käärik in the Institute of Chemistry, University of Tartu. The Raman spectroscopy measurements were carried out by Dr. Alexey Treshchalov in the Institute of Physics, University of Tartu. The X-ray diffraction (XRD) analysis was conducted by Jaan Aruväli in the Institute of Ecology and Earth Sciences, University of Tartu. The X-ray photoelectron spectroscopy (XPS) measurements were carried out by Dr. Arvo Kikas in the Institute of Physics, University of Tartu.

For SEM studies, the catalyst materials' suspensions in 2-propanol were pipetted onto polished glassy carbon (GC) substrates and dried at 60 °C. The Helios NanoLab 600 (FEI Company) high-resolution scanning electron microscope was used. The elemental composition of the samples was determined using the INCA Energy 350 EDX spectrometer (Oxford Instruments), which was attached to this microscope.

Studies using scanning transmission electron microscopy (STEM) were performed at 200 kV on a Titan Themis 200 (FEI) (S)TEM equipped with a Cs-probe corrector. With the help of the SuperX EDX system (Bruker), the EDX mapping was performed. Drop-casting the catalyst material in 2-propanol onto lacey carbon film-coated copper TEM grids was used to prepare the sample for STEM investigation.

The porous structure of the catalyst materials was characterised using low-temperature N_2 physisorption analysis with NOVA touch LX2 (Quantachrome Instruments). The samples were degassed in vacuum at 300 °C for 12 h before measurements. The specific surface area (S_{dft}) of materials, the volume of micropores (V_{μ}) and the pore size distribution were calculated from N_2 adsorption/desorption isotherms using a quenched solid density functional theory (QSDFT) equilibria model for slit type pores. Brunauer-Emmett-Teller (BET) surface area (S_{BET}) was calculated at relative pressure (P/P_0) between 0.02 - 0.2. The total pore volume (V_{tot}) was calculated at P/P_0 of 0.97.

X-ray diffraction (XRD) measurements were carried out with a Bruker D8 Advance diffractometer using Ni-filtered Cu K_{α} radiation. With scanning steps of 0.0126° 2θ in the range of 5° to 89° and a counting time of 525 s per step, the diffraction patterns were acquired. Software Topas 6 (Bruker) was used to analyse the data.

Raman spectroscopic technique was used to characterise the catalyst materials. All samples were suspended in water and drop-coated on silicon substrates. Micro-Raman spectra were recorded in the back-scattering geometry on an inVia Renishaw spectrometer in conjugation with a confocal microscope (Leica Microsystems CMS GmbH), 50X objective and an argon ion laser operated at 514.5 nm. Low incident laser power density at the sample prevented excessive sample heating and/or decomposition, while allowing getting averaged information over ~200 μm^2 area in a single exposure.

A non-monochromatic twin anode X-ray tube (Thermo XR3E2) with a characteristic energy of 1,253.6 eV (Mg K_{α}) and an electron energy analyzer SCIENTA SES 100 were used for the X-ray photoelectron spectroscopy (XPS) study under ultra-high vacuum conditions. The survey spectra were collected by five scans with a pass energy of 200 eV, step size of 0.5 eV, step time of 0.2 s, and energy range from 900 to 0 eV. At least 25 scans of a detailed spectrum were

taken, each having a step size of 0.1 eV and a step duration of 0.2 s. The K_α and K_β satellites were taken out of the data processing process using CasaXPS (version 2.3.17). Peak fitting was performed using a blend of linear and Shirley-type backgrounds and the Gauss-Lorentz hybrid function (GL 70, Gauss 30 %, and Lorentz 70 %).

2.3. Electrochemical characterisation

GC discs (cut from GC-20SS rod, Tokai Carbon Ltd., Japan) fitted in Teflon holders were employed as a substrate material for the rotating disc electrode (RDE) experiments. The geometric area of the electrode (*A*) was 0.196 cm^2, which was used to calculate the current densities reported in this thesis. The GC electrode was cleaned by sonication in Milli-Q water and 2-propanol for 5 min in each solvent before being polished to a mirror shine using 1 and 0.3 μm alumina slurries (Buehler).

4 mg of catalyst material were dispersed in 490 μl of 2-propanol and 490 μl of Milli-Q water, and 20 μl of Nafion ionomer solution (5 wt.%, Sigma-Aldrich) was added to prepare a catalyst suspension. The suspensions were sonicated in an ultrasonic bath until uniform dispersions were attained, which took at least 4 h. A certain amount of catalyst suspension was pipetted onto the cleaned GC surface in order to achieve a catalyst loading of 0.2 mg cm^{-2} (for the measurements in 0.1 M KOH) or 0.8 mg cm^{-2} (for the measurements in 0.5 M H_2SO_4). The catalyst layer was then allowed to dry in air at 60 °C. For coating the electrodes with a commercial Pt/C catalyst (20 wt. %, E-TEK), the same procedure was used.

All electrochemical tests were carried out in a three-electrode glass cell in 0.1 M KOH (purity 85%, Sigma-Aldrich) or 0.5 M H_2SO_4 (96-97% Puriss p.a analytical grade) solutions. The electrolyte solution was saturated with either Ar (99.999%, Linde Gas) or O_2 (99.999%, Linde Gas), and a steady flow of the gas was maintained over the solution during the experiment. The working electrode was the GC disc coated with an appropriate catalyst. As a reference electrode, a saturated calomel electrode (SCE) was used. A glass frit served as the barrier separating the working electrode compartment from the auxiliary electrode, which was a carbon rod. The electrochemical measurements were carried out using a Metrohm-Autolab PGSTAT30 potentiostat/galvanostat (The Netherlands). An EDI101 rotator (Radiometer) was attached to a CTV101 speed control unit that was used to regulate the different electrode rotation rates (ω) of 360-3100 rpm.

The RDE data was analysed using the Koutecky-Levich equation [62]:

$$\frac{1}{I} = \frac{1}{I_k} + \frac{1}{I_d} = \frac{1}{I_k} + \frac{1}{0.62nFAD_{O_2}^{2/3}\nu^{-1/6}C_{O_2}^{b}\omega^{1/2}} \quad (7)$$

where I is the measured current, I_k and I_d are the kinetic and diffusion-limited currents, respectively, n is the number of electrons transferred per O_2 molecule, F is the Faraday constant (96485 C mol^{-1}), A is the geometric electrode area, ω is the electrode rotation rate (rad s^{-1}), $C_{O_2}^{b}$ is the concentration of oxygen in the bulk (1.2×10^{-6} mol cm^{-3} in 0.1 M KOH) [63], D_{O_2} is the diffusion coefficient of oxygen (1.9×10^{-5} cm^2 s^{-1} in 0.1 M KOH) [63] and ν is the kinematic viscosity of the solution (0.01 cm^2 s^{-1}). For the experiments carried out in acidic solution, the following constants were used: $C_{O_2}^{b}$ =1.13×10^{-6} mol cm^{-3} and D_{O_2} = 1.8×10^{-5} cm^2 s^{-1} [64].

The short-term stability testing of catalyst materials was carried out by applying 10 000 potential cycles at 200 mV s^{-1} in O_2-saturated 0.1 M KOH solution, while the RDE polarization curves at 10 mV s^{-1} and 1900 rpm were recorded before and after the potential cycling.

The AEMFC tests were conducted by John C. Douglin at the Wolfson Department of Chemical Engineering, Technion-Israel Institute of Technology (Israel). To evaluate the performance of FeNC(Mg) and FeCoNC(Mg) catalysts in anion-exchange membrane fuel cells (AEMFCs), gas diffusion electrodes (GDEs) of 2.25 cm^2 were made in a manner similar to previous publications [29][65][66][67][68]. For the anodes, ~22 mg of powdered anion-exchange ionomer (Fumion®, Fumatech) was added to a mortar and ground for 3 min. Following the initial grind, 61 mg of PtRu/C (40% Pt and 20% Ru on carbon black HiSPEC 10000, Alfa Aesar) was added to the mortar along with an additional 30 mg of carbon black (Vulcan XC-72) to increase the porosity and hydrophobicity of the catalyst layer and ultimately avoid flooding. 1 ml of deionized water and 9 mL of 2-propanol were added to the solid mixture and further ground for 10 min to create a low viscosity catalyst ink. The FeNC(Mg) and FeCoNC(Mg) cathode inks were prepared in a similar manner to the anode ink, wherein 13 mg of ionomer were first added and ground, followed by adding 20 mg of each catalyst. Ten millilitres of total solvents were added to each mortar and ground for an additional 10 min.

The catalyst inks were sonicated for 1 h in an ice-cooled ultrasonic bath. Following sonication, the cathode inks were sprayed directly onto 2.25 cm^2 Toray Carbon Paper 060 (Fuel Cell Store) with microporous layer GDLs with an Iwata HP-TH professional airbrush. The loadings for the FeNC(Mg) and FeCoNC(Mg) GDEs were 0.62 mg_{MNC} cm^{-2} (M = Fe or FeCo). The anode ink was spray deposited onto a 6.05 cm^2 Toray Carbon Paper 060 GDL with 5% wet-proofing.

Upon arriving at a PGM loading of 0.75 mg_{PtRu} cm^{-2}, two smaller 2.25 cm^2 GDEs were cut from the larger 6.05 cm^2 GDE.

Two 5 cm^2 pieces of FAA-3-05-RF AEM (Fumatech) and all electrodes were immersed in 1 M KOH aqueous solution for 1 h prior to cell assembly, with solution changes every 20 min before testing. Two different AEMFCs were assembled between two 5 cm^2 single-serpentine graphite bipolar flow field plates with Teflon gaskets and torqued to 4.5 N m to achieve an average GDL compression of 30%. The cells were tested under H_2/O_2 gas flows of 0.5 SLPM at cell temperatures of 60 and 80 ^oC with 100 kPa of back-pressurization in an 850E Scribner Associates Fuel Cell test station.

3. Results and discussion

3.1. Physicochemical characterization

The surface morphology of the manufactured catalyst materials was characterized using the SEM method, and the resulting micrographs are shown in Figure 4. Based on the micrographs, it is evident that all the materials have a rather similar morphology and consist of irregular, sheet-like carbon structures. The Fe-containing catalysts prepared with the MgO template (Figure 4e and 4f) and without template (Figure 4c and 4d) do not appear to differ significantly in SEM micrographs and have similar morphology to the catalysts prepared from alkylresorcinols using a similar method [25].

All the catalyst materials have layered heterogeneous sheet-like structures, which may be due to the presence of DCDA in the synthesis process. The DCDA performs two roles: it helps to create the porous structure and it adds nitrogen atoms as dopants. During the pyrolysis, DCDA polymerises between 300 and 600 °C, creating layers of graphitic carbon nitride (g-C_3N_4) [69]. Between these layers, the carbon precursor is imprisoned. g-C_3N_4 decomposes into reactive gaseous nitrogen species as the temperature rises, adding nitrogen to the newly created carbon framework [70].

STEM was used for more precise characterization of catalysts and elemental distribution (Figure 5). The STEM-EDX mapping of the catalysts FeNC(Mg) and FeCoNC(Mg) show that both catalysts have homogeneous dispersion of N element throughout the material (Figures 5f and 5m), verifying successful nitrogen doping. From Figures 5e and 5l it is apparent that a part of the transition metals is evenly distributed over the carbon support, presumably as nitrogen-coordinated atomically dispersed metal centres (M-N_x). However, it is evident that both catalyst materials also contain metal-rich nanoparticles, which are encapsulated in graphitic carbon shells (Figure 5b and 5i). In bimetallic catalysts, these nanoparticles consist of both iron and cobalt (Figure 5l). It is also evident that the materials contain some evenly distributed Mg even after acid washing, but no MgO nanoparticles (Figure 5g and 5n).

The specific surface area of the catalysts was determined by N_2 physisorption analysis. The addition of Mg acetate significantly increases the specific surface area of Fe-based materials, which is 345 $m^2\ g^{-1}$ and 483 $m^2\ g^{-1}$ for FeCN and FeCN(Mg) catalysts, respectively (Table 1). It is evident that both the total pore volume (V_{tot}) and the micropore volume (V_{μ}) were higher for the catalyst materials prepared using the template. Bimetallic catalyst, however, had lower specific surface area and pore volume. From the pore size distribution graph (Figure 6) it can be seen that all catalysts contain mesopores of different sizes. The hierarchically porous

structure of these materials could be beneficial to the application in the fuel cells, as the mesopores promote O_2 transport and product diffusion, as well as increase the contact area between the electrolyte and active sites on the on the surface of the catalyst.

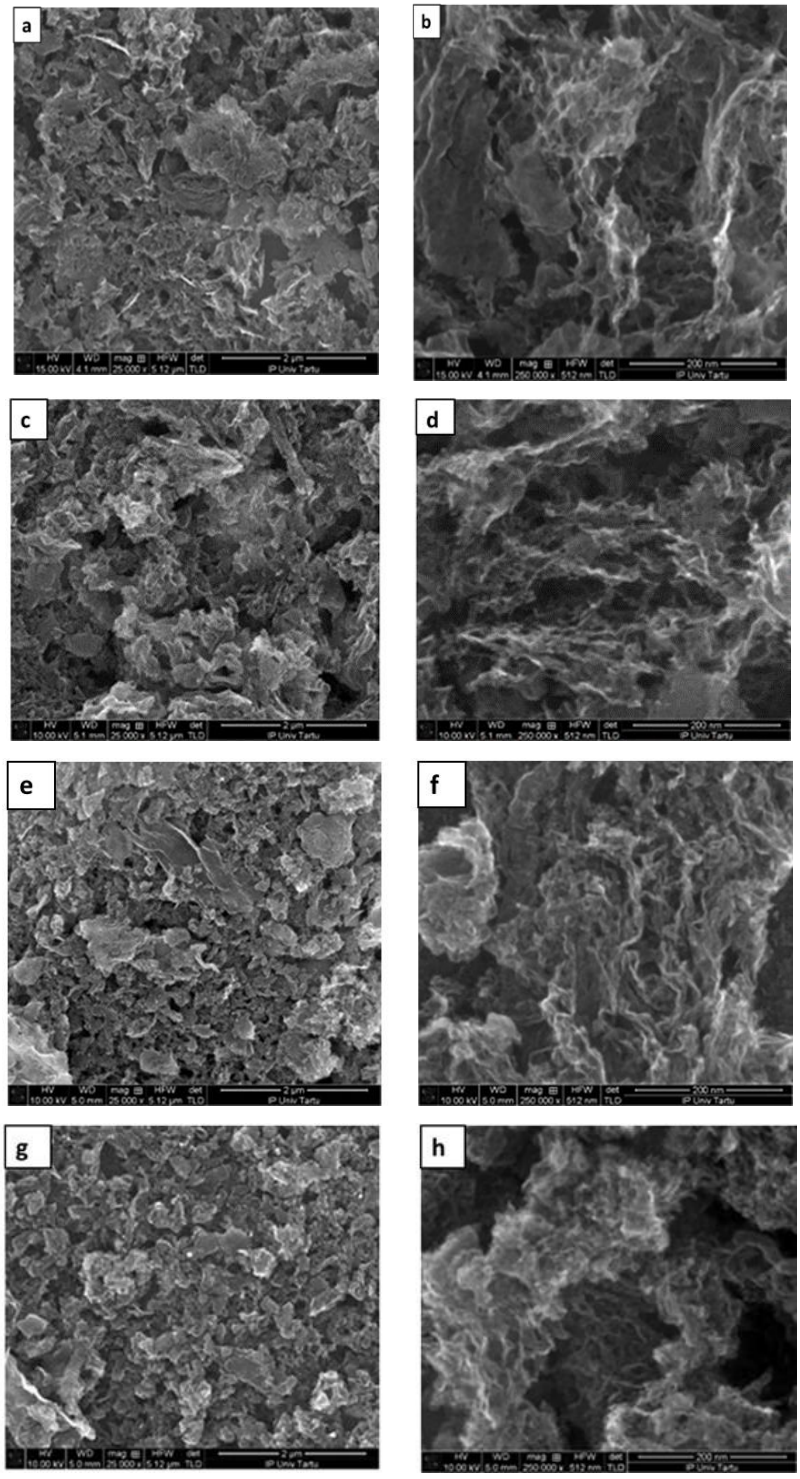

Figure 4: SEM images of (a, b) NC(Mg); (c,d) FeNC; (e,f) FeNC(Mg); (g,h) FeCoNC(Mg) catalysts.

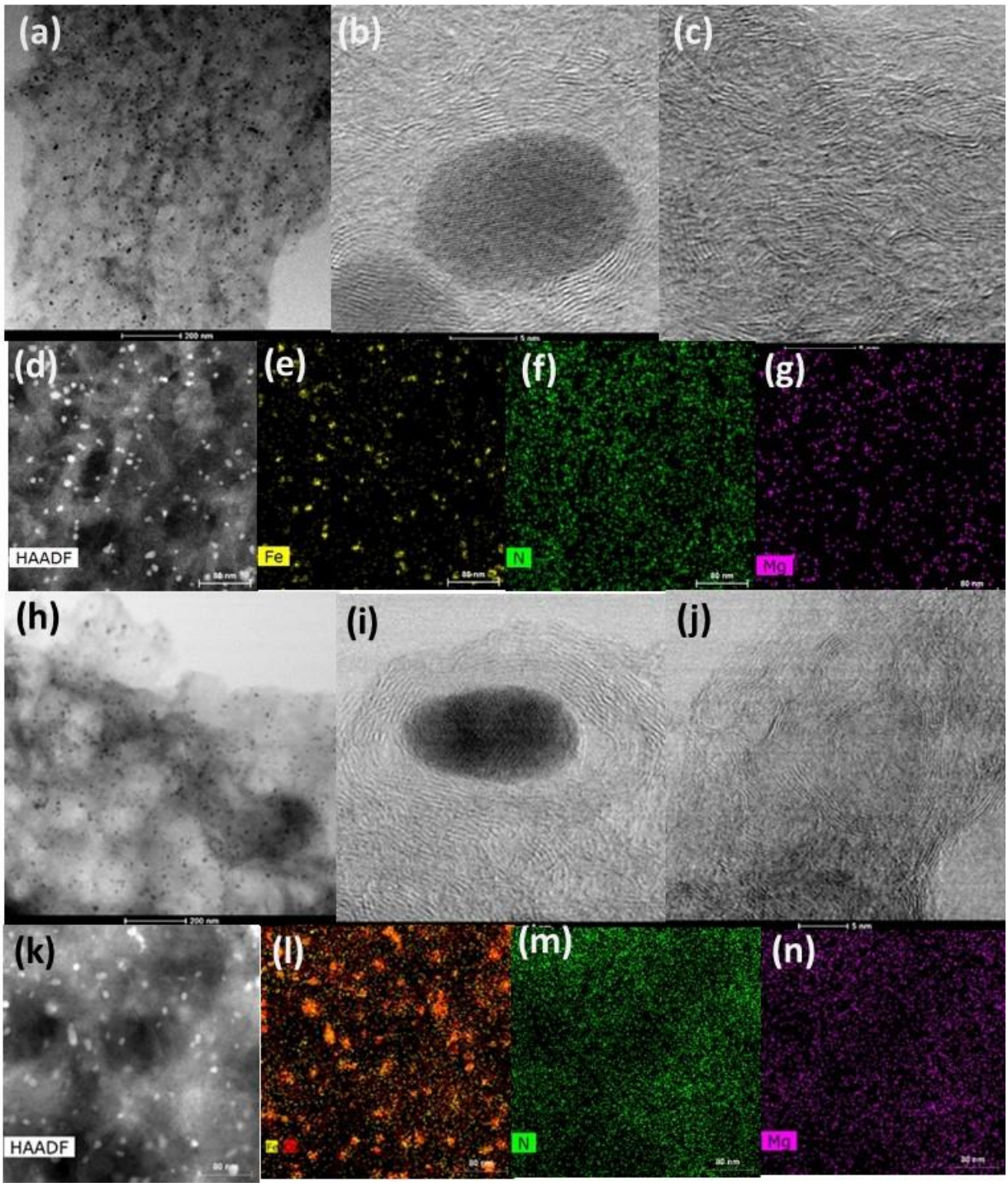

Figure 5: (a–c) STEM micrographs with different magnifications of the FeNC(Mg) material, (d) High-angle annular dark-field (HAADF)-STEM image of FeNC(Mg) material with respective EDX elemental mapping images (e-g). (h-j) STEM micrographs with different magnifications of the FeCoNC(Mg) material, (k) High-angle annular dark-field (HAADF)-STEM image of FeCoNC(Mg) material with respective EDX elemental mapping images (l-n).

Table 1. Specific surface area, total pore volume and micropore volume of the catalysts.

Catalyst	S_{BET} (m^2 g^{-1})	S_{dft} (m^2 g^{-1})	V_{μ} (cm^3 g^{-1})	V_{tot} (cm^3 g^{-1})
FeNC	345	339	0.09	0.54
FeNC(Mg)	483	433	0.14	0.61
FeCoNC(Mg)	203	195	0.05	0.32

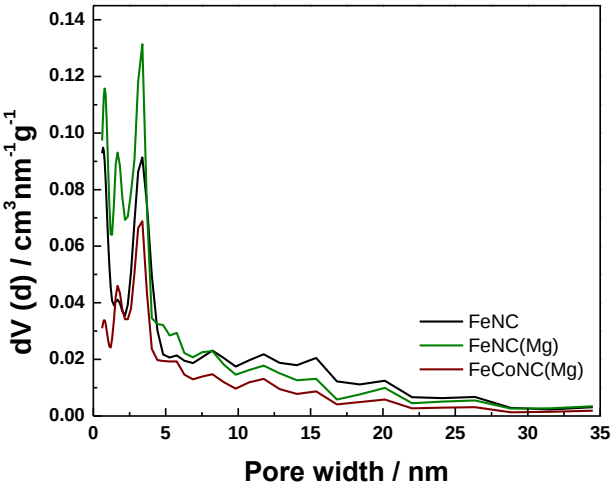

Figure 6: Pore size distribution of catalysts.

The XRD analysis (Figure 7a) revealed that nanoparticles in FeNC(Mg) consist mostly of Fe_3C (cohenite) and in FeCoNC(Mg), of FeCo alloy with the Fe/Co atomic ratio close to 1 (wairauite). The estimated contents of Fe_3C and FeCo in the catalysts are 1.3 wt.% and 0.7-0.8 wt.%, respectively. According to the full profile analysis, the carbon can be considered to be partly graphitic (ca. 70%) and partly amorphous (ca. 30%).

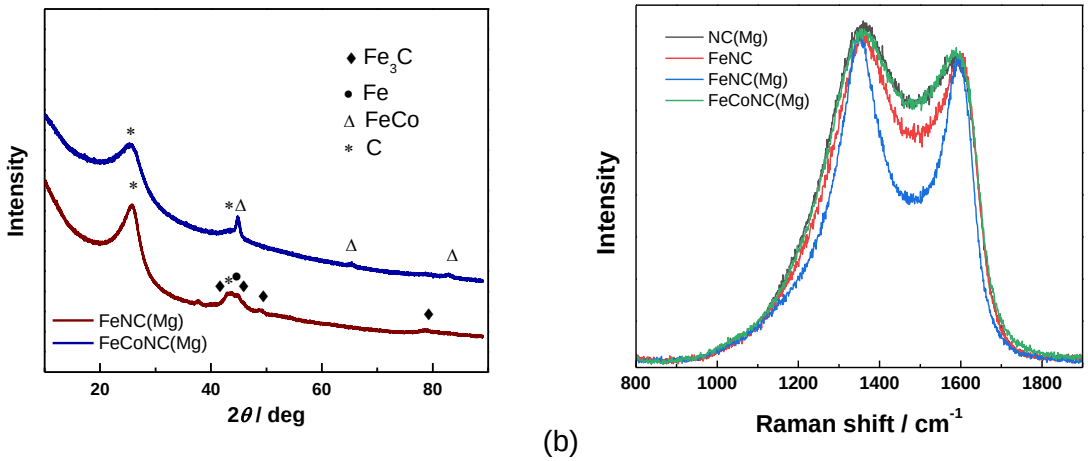

(a) (b)

Figure 7: (a) XRD pattern of FeNC(Mg) and FeCoNC(Mg), (b) Raman spectra of catalysts.

The Raman spectra (Figure 7b) were fitted following the four-peak model where G peak (~1590 cm^{-1}) corresponds to the stretching vibrations of the sp^2 carbon atoms in the ideal graphitic lattice; D1 (~1350 cm^{-1}) to defect-activated breathing mode of aromatic rings; D3 (~1490 cm^{-1}) to amorphous carbon and D4 (~1100 cm^{-1}) to disordered graphitic lattice A baseline correction was used to compensate for the small fluorescence background and multiple-peak fitting procedure was applied using the PeakAnalyser software in OriginPro 9. The intensities of I_{D1} and I_G (integrated areas under the bands) as well as their full widths at half-maxima were extracted from the fitting of the curves by Voigt functions. In the curve-fitting procedure, all parameters (peak position, height, and width) were adjusted to attain the smallest value of the chi-square. The widths of the G band (W_G) and especially D1 band (W_{D1}) are qualitative measures of structural disorder for defective carbon materials [71]. To determine the extent of structural disordering in the catalyst materials, the I_{D1}/I_G ratio was determined. It should be highlighted, nevertheless, that the I_{D1}/I_G Raman band ratio, which is frequently utilized, is not appropriate for highly disordered carbon materials, as the G peak in such materials is a superposition of the G and D2 peaks. From the results listed in Table 2 it can be concluded that the prepared catalysts have quite defect rich nature. It is interesting to note that Fe-based materials, especially FeNC(Mg) contain least defects in graphitic structures (narrowing of D1 and G bands). It is well known that Fe species serve as good catalyst for the growth of highly graphitized carbon materials during pyrolysis [72].

SEM-EDX was used to determine the elemental composition of the various catalyst materials (Table 3). It should be noted that the Fe content encompasses all types of Fe found in the catalyst, including metal Fe, Fe oxides, nitrogen-coordinated Fe, and Fe carbides. The Fe content is higher in FeCN as compared to FeCN(Mg) and FeCoCN(Mg), as the acid treatment with HCl for removal of MgO template also dissolves the metal-containing nanoparticles that are not encapsulated. It can also be seen that Mg is detected in the materials prepared with template, indicating that acid treatment does not remove all of it. The EDX analysis also showed traces of some other elements, like Si, Cl, F, Na, and Ca.

Table 2. Full width at half-maximum (FWHM) values of the D1 and G-bands in Raman spectra and I_{D1}/I_G ratio.

Catalyst	**W_{D1} / cm^{-1}**	**W_G / cm^{-1}**	**I_{D1}/I_G**
NC(Mg)	240	112	4.7
Fe(NC)	226	94	4.8
FeNC(Mg)	150	84	3.1
FeCoNC(Mg)	246	108	4.7

Table 3: Elemental composition (wt%) of catalyst materials determined by SEM-EDX.

Catalyst	**C**	**N**	**O**	**Mg**	**Fe**	**Co**
NC(Mg)	68.0±5.3	19.4±1.3	8.9±2.1	3.1±1.8		
FeNC	49.5±1.7	19.4±3.2	16.9±1.7		12.2±4.4	
FeNC(Mg)	79.5±2.57	7.5±0.4	7.8±1.1	0.6±0.4	3.2±1.1	
FeCoNC(Mg)	67.6±2.0	14.2±2.5	9.0±1.3	2.1±0.5	2.9±0.9	2.9±1.0

The XPS analysis (Table 4, Figure 8) also revealed the presence of carbon, nitrogen, oxygen, iron, cobalt and magnesium on the catalyst materials' surface. Unsurprisingly, the surface metal concentration was higher for the untreated catalysts, because acid leaching removes transition metal-containing nanoparticles not enclosed in carbon. Intriguingly, compared to the FeCN(Mg) material, the bimetallic catalyst had higher surface metal and nitrogen contents. The comprehensive N 1s spectra were deconvoluted into seven sub-peaks (Figure 8b) to evaluate the presence of various N species in the catalysts and the relative content of N species is provided in (Table 5). The most prevalent N species in all catalysts is pyridinic-N, but significant levels of hydrogenated-N (including pyrrolic-N and hydrogenated pyridine), graphitic-N, and metal-coordinated N were also found. The ORR has been demonstrated to be catalysed by graphitic-N and pyridinic-N. The development of strong chemical interactions between carbon and oxygen atoms is encouraged by graphitic-N groups, which may reduce the activation energy of the ORR and boost the dissociation of O_2 molecules on nearby carbon atoms [23]. Pyridinic-N content is frequently linked with the ORR activity [73]. It has been demonstrated that M-N_x centres have the highest ORR activity of these catalysts, particularly in acidic solutions but also in alkaline medium [73]. However, it is still unclear which N-functionality or the chemical makeup of nitrogen-containing active sites actually drives the ORR activity.

The detailed Fe 2p spectrum (Figure 8a, inset) consists of several peaks corresponding mostly to oxidised forms of iron, which could be N-coordinated atomically dispersed metal centres, but also some metal oxides. The exact identification of these peaks is not possible, because of multiple overlapping peaks, which are due to charge transfer effects and multiplet splitting [74]. The deconvolution of detailed O 1s and C 1s spectra reveals the existence of various functional groups with C-O and C-N bonds on the surface [75] as shown in Figures 8c and 8d.

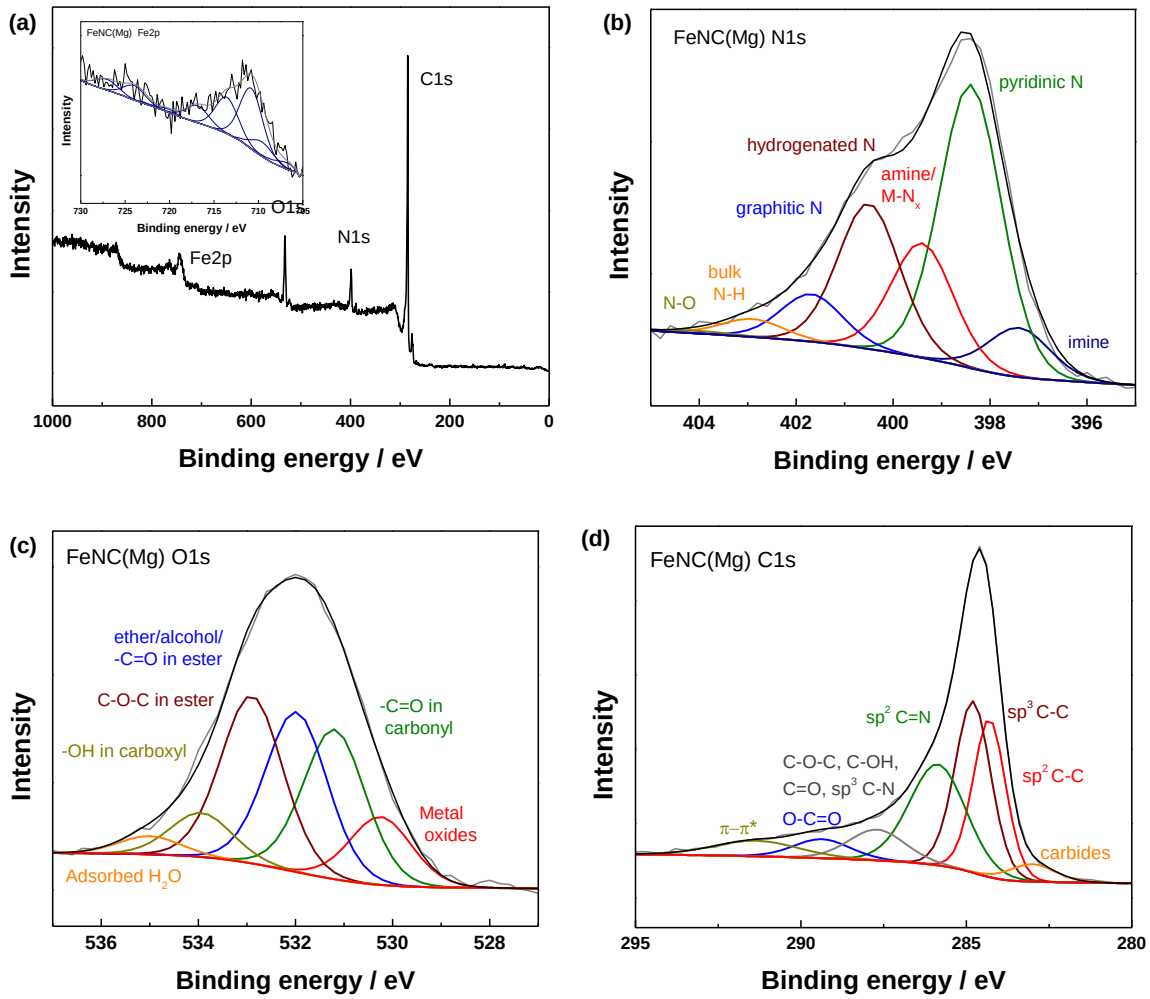

Figure 8. (a) XPS survey spectrum and detailed Fe2p spectrum (inset); (b) detailed N1s spectrum; (c) O1s spectrum and (d) C1s spectrum of FeNC(Mg) catalyst material.

Table 4: Surface elemental composition (at%) of catalysts by XPS analysis

Catalyst	C	N	O	Fe	Co	Mg
NC(Mg)	70.4	15.0	10.9	0.0	0.0	3.7
FeNC	71.5	14.9	11.7	2.0	0.0	0.0
FeNC(Mg)	82.2	7.4	8.8	0.3	0.0	1.3
FeCoNC(Mg)	78.7	10.1	8.8	0.4	0.8	1.1

Table 5: Relative concentration (%) of N species by XPS analysis

Catalyst	Imine	Pyridinic N	Amines/ M-N$_x$	Hydroge-nated N	Graphi-tic N	bulk N-H	N-O
NC(Mg)	5.2	51.1	12.2	21.5	7.2	2.2	0.5
FeNC	5.2	44.6	17.9	21.2	8.7	2.1	0.3
FeNC(Mg)	7.5	42.9	17.4	22.0	7.2	2.7	0.4
FeCoNC(Mg)	6.5	42.8	17.3	20.2	9.7	2.7	0.9

3.2. Rotating disk electrode results

RDE was used for the initial evaluation of electrocatalytic activity of the carbon-based catalysts towards the ORR in an aqueous 0.1 M KOH electrolyte. The RDE polarization curves were recorded at different electrode rotation rates (Figure 9) and the data was analysed using the Koutecky-Levich (K-L) equation (Eq. 7). The intercept of extrapolated K-L lines (Figure 9b) is near zero at the potentials E<-0.5 V, thus indicating that the electroreduction of O_2 is under the diffusion control in a broad range of potentials for catalyst. The number of electrons transferred (*n*) was calculated from the slopes of the K-L plots. It can be seen from the inset of Figure 9b that the *n* value is close to 4 at all potentials for this material. These results show that the electroreduction of O_2 proceeds predominantly via direct $4e^-$ pathway (Eq. 4) or $2+2e^-$ pathway, where peroxide anion is further reduced to OH^- (Eqs. 5 and 6)

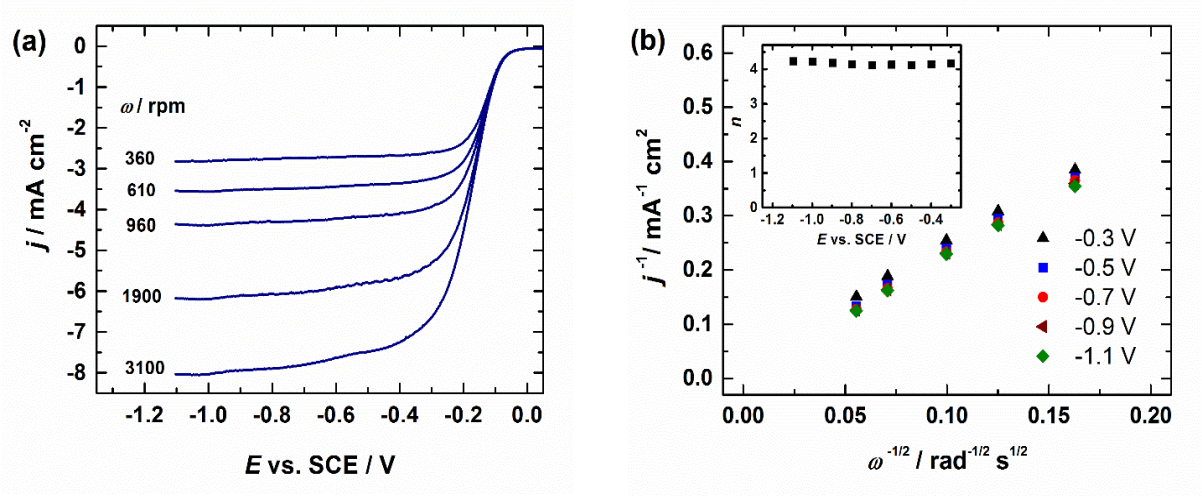

Figure 9: (a) RDE voltammetry curves for the ORR on FeNC(Mg) catalyst at various rotation rates (v=10 mV s^{-1}). (b) Koutecky-Levich plots for the ORR derived from the RDE data. Inset shows the value of *n* as a function of potential.

To find the optimal Fe content of the catalysts, it was varied in the catalyst preparation. The RDE voltammograms at 1900 rpm of the catalysts prepared using different content of Fe salt are compared in Figure 10a. The values of onset potential (E_{onset} – the potential at which the ORR current density reaches -0.1 mA cm^{-2}) and half-wave potentials ($E_{1/2}$ – the potential at which the ORR current density is half of the value of j_d) found from the RDE data are presented in Table 6. It is evident that the metal-free catalyst shows the lowest electrocatalytic activity and that both the $E_{1/2}$ and E_{onset} values increase with increasing the amount of the Fe salt added in the catalyst preparation. The most active electrocatalyst appears to be FeNC(Mg) and further increase of the Fe content does not result in increasing the ORR activity.

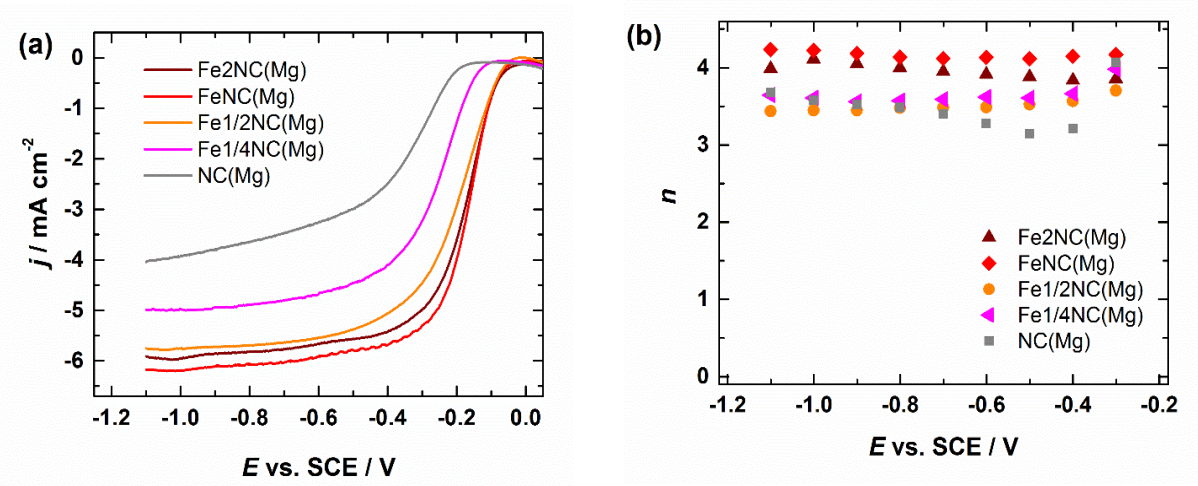

Figure 10: Comparison of ORR polarisation curves recorded in O_2-saturated 0.1 M KOH solution on Fe-containing catalysts with different Fe content (ν=10 mV s^{-1}, ω=1900 rpm, catalyst loading 0.2 mg cm^{-2}). (b) Value of *n* as a function of potential for various catalysts.

Table 6: The kinetic parameters of ORR in 0.1 M KOH from RDE measurements.

Catalyst	$E_{1/2}$ **vs. SCE / V**	E_{onset} **vs. SCE / V**	**MA at -0.2 V / A** g^{-1}
NC(Mg)	-0.35	-0.20	0.5
Fe1/4NC(Mg)	-0.25	-0.12	9.2
Fe1/2NC(Mg)	-0.20	-0.05	31
FeNC(Mg)	-0.17	-0.05	61
Fe2NC(Mg)	-0.18	-0.05	49
FeCoNC(Mg)	-0.21	-0.06	23
FeNC	-0.21	-0.09	38
Pt/C	-0.18	-0.04	47*

*per total catalyst mass

The values of mass activity (MA) for ORR were calculated for the catalysts at -0.2 V vs SCE:

$$MA = I_k / m \quad (8)$$

where I_k is the kinetic current at this potential, which was calculated from K-L equation (Eq. 7) and *m* is the mass of the catalyst on the electrode. It can be seen that the mass activity again increases with increasing the Fe content in the catalysts, is the highest for FeNC(Mg), and slightly smaller for the catalyst of highest Fe content. It can be assumed that there is an optimal Fe content in the catalyst that yields the highest number of ORR-active Fe-N_x centres, and further increasing the Fe content just increases the amount and/or size of Fe-containing nanoparticles and may even decrease the content of the Fe-N_x sites that are accessible to O_2 molecules. For FeNC(Mg), the mass activity calculated at -0.1 V vs SCE was 4.5 A g^{-1}, which

is comparable to the value obtained for an iron-containing catalysts prepared from metal organic framework [76], but slightly smaller as compared to those of transition metal-containing carbon catalysts prepared from commercial mesoporous support materials [77].

In Figure 10b, the dependence of *n* value on *E* is shown for the catalysts presented in Figure 10a. The smallest *n* values, between 3 and 3.5, are observed for transition metal-free catalyst NC(Mg). This indicates partial reduction of O_2 to HO_2- anions on this catalyst and may be due to the absence of M-N_x centres that catalyse 4e$^-$ reduction of O_2 [78]. The *n* values generally increase with increasing the Fe content in the catalysts and highest *n* was observed for the most active catalyst, FeNC(Mg) which presumably has the highest number of active sites capable of either 4e$^-$ reduction of O_2 and/or further reduction of peroxide anion.

In Figure 11, the RDE polarisation curves FeNC(Mg) are compared with those of bimetallic catalyst and catalyst prepared without magnesium template (FeCN), as well as with that of commercial Pt/C. It can be seen that the bimetallic catalyst has slightly lower ORR activity and also lower *n* value as compared to FeNC(Mg). Similar results were observed with the catalysts prepared from alkylresorcinols using a similar method [43]. Higher activity of FeNC(Mg) may be related to its higher specific surface area or favourable porous structure due to using the template, which increases the number of accessible active sites. It can also be seen that the activity of FeNC(Mg) is similar to that of commercial Pt/C catalyst.

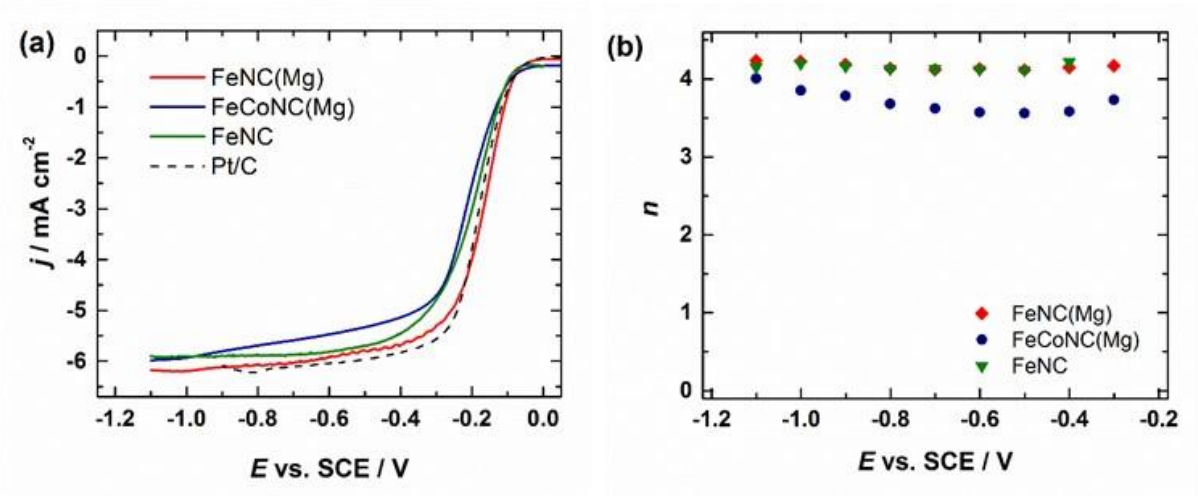

Figure 11: (a) Comparison of ORR polarisation curves recorded in O_2-saturated 0.1 M KOH solution for FeCN(Mg), FeNC, FeCoNC(Mg) and Pt/C catalysts (v=10 mV s^{-1}, ω=1900 rpm, catalyst loading 0.2 mg cm^{-2}). (b) Value of *n* as a function of potential for various catalysts.

M–N–C catalysts are generally more durable in alkaline media as compared to acidic media due to the lower propensity for 3d metal dissolution, but carbon corrosion is still a concern as it impacts the structure of the carbon framework and causes the degradation of active centres

[79]. Thus, the low electrochemical stability of the electrocatalysts is one of the major obstacles to long-term AEMFC operation. To evaluate the durability of FeNC(Mg) and FeCoNC(Mg), the catalyst materials were subjected to accelerated stability tests by potential cycling (Figure 12). Both electrocatalysts demonstrated high stability, as for both FeNC(Mg) and FeCoNC(Mg) catalysts the $E_{1/2}$ shifted to negative direction only by 6 mV and E_{onset} only by 8 mV after 10000 potential cycles. The good stability could be caused by the high degree of graphitization as confirmed by both Raman spectroscopy and XRD analysis.

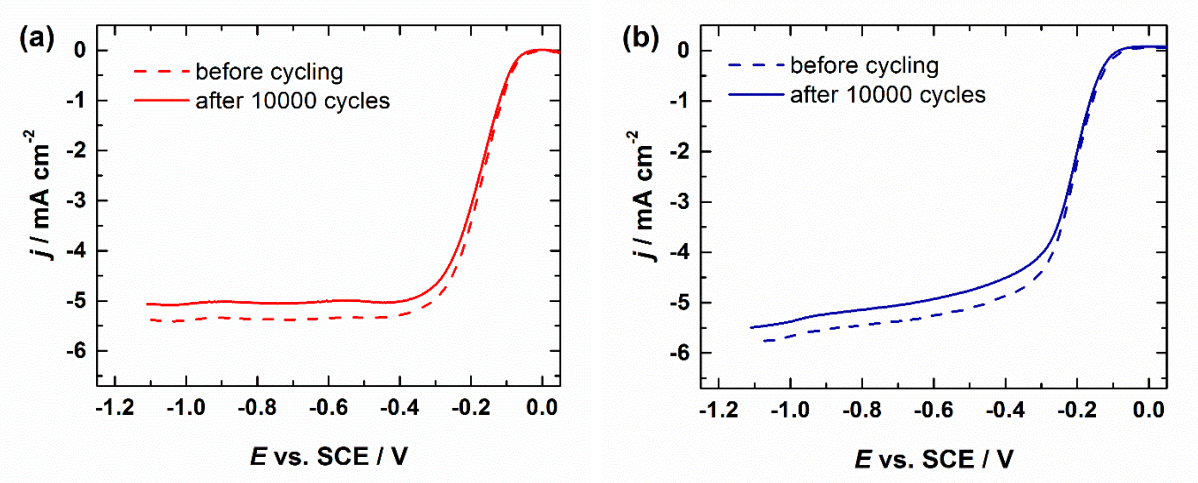

Figure 12: RDE voltammetry curves for ORR on (a) FeNC(Mg) and (b) FeCoNC(Mg) catalysts in O_2-saturated 0.1 M KOH solution before and after 10,000 potential cycles (ω=1900 rpm, ν=10 mV s^{-1}).

For the templated materials FeNC(Mg) and FeCoNC(Mg) the RDE tests were also conducted in 0.5 M H_2SO_4 solution (Figure 13). Both of these showed reasonably good ORR activity, with the values of $E_{1/2}$=0.47 V and E_{onset}=0.59 V. As compared to commercial Pt/C catalyst, however, these values were still about 90 mV more negative.

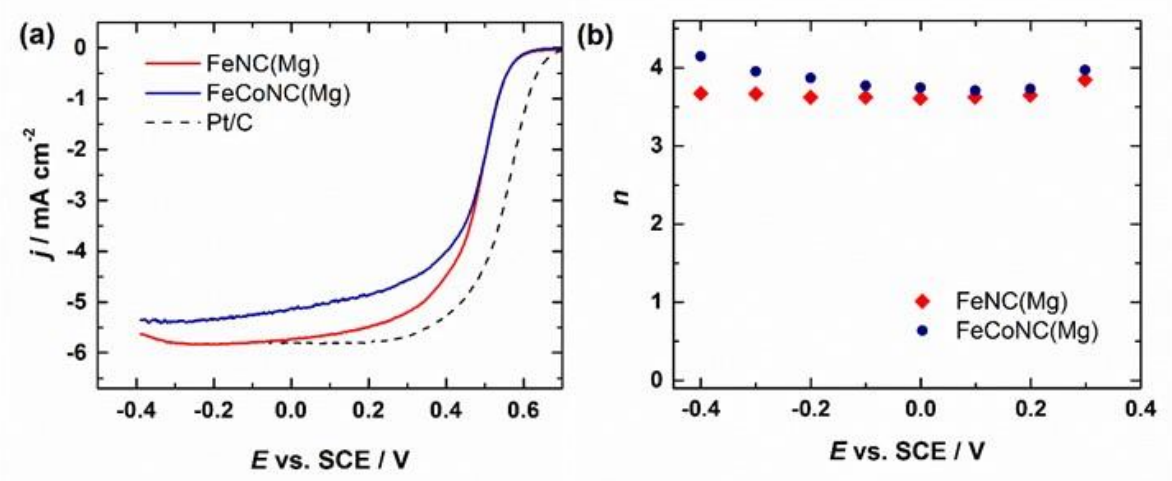

Figure 13: (a) Comparison of ORR polarisation curves recorded in O_2-saturated 0.5 M H_2SO_4 solution on FeCN(Mg) and FeCoNC(Mg), and Pt/C catalysts (ν=10 mV s^{-1}, ω=1900 rpm, catalyst loading 0.8 mg cm^{-2}). (b) Value of *n* as a function of potential for various catalysts.

3.3. AEMFC tests

The H_2/O_2 polarization curve results of AEMFCs based on the FeNC(Mg) and FeCoNC(Mg) bimetallic ORR catalysts are shown in Figure 14. To accurately compare the performances of the catalysts as cathodes, the operating conditions were kept the same in all instances. With the cell temperature at 60 °C and anode and cathode dewpoint temperatures set to 57 and 58 °C, respectively with 100 kPa of back-pressurisation, the cell made with FeCoNC(Mg) exhibited a higher P_{max} (675 mW cm^{-2}) than the cell made with FeNC(Mg) (Figure 14a). Furthermore, the FeCoNC(Mg) cell arrived at ten times higher current density value at 0.8 V (263 vs 28 mA cm^{-2}). Upon increasing the cell temperature to 80 °C, anode and cathode dewpoint temperatures to 76 and 77 °C, respectively and maintaining 100 kPa of back-pressurisation, the P_{max} performances increased to 833 and 615 mW cm^{-2}, once again in favour of the FeCoNC(Mg) (Figure 14b). Likewise, the catalytic region activity of the FeCoNC(Mg) cell was higher, but arrived at approximately the same values as the 60 °C temperature condition.

The reason why FeCoNC(Mg) material showed higher activity on the AEMFC despite of its lower activity in RDE test is not clear at present. However, higher AEMFC performance and lower RDE activity of bimetallic FeCo catalyst as compared to similar Fe-containing material has been observed before [65] and it was attributed to the synergistic effect of Fe-N_4 and Co-N_4 centres [32]. Comparison of AEMFC performance of FeCoNC(Mg) and FeNC(Mg) catalysts with the results of other biomass-derived non-precious metal catalysts reported in the literature places the materials obtained in this work among the best performing AEMFC cathode catalysts (Table 7).

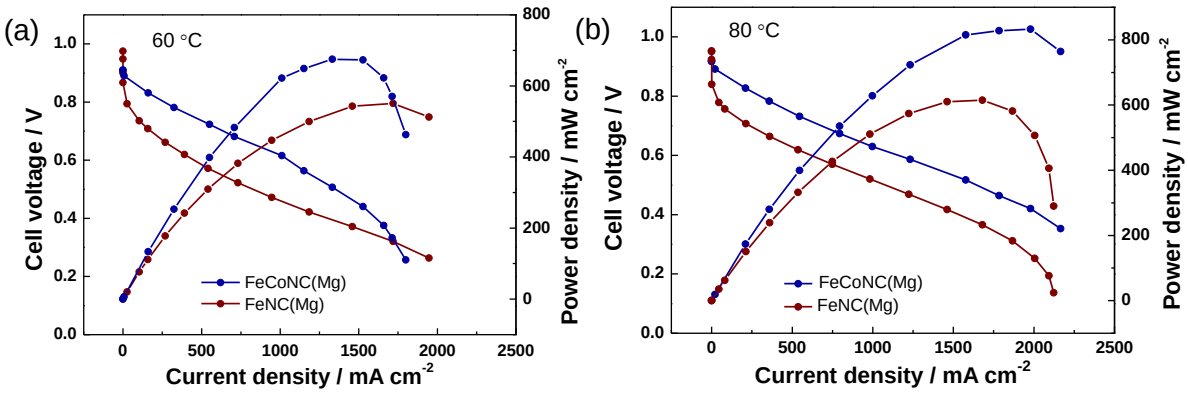

Figure 14: Polarization and power density curves for H_2/O_2 AEMFCs at (a) 60 °C and (b) 80 °C. Anode catalyst: PtRu/C and cathode catalysts: FeCN(Mg) and FeCONC(Mg).

Table 7. AEMFC performance of various biomass-derived cathode materials.

Cathode catalyst	Biomass source	Cathode loading (mg cm^{-2})	Anode loading (mg cm^{-2})	T (°C)	Membrane	P_{max} (mW cm^{-2})	Ref.
FeCoNC(Mg) FeNC(Mg)	lignin	0.62 0.62	0.75 PtRu 0.75 PtRu	60 60	FAA-3-05-RF	675 550	This work
FeCoNC(Mg) FeNC(Mg)	lignin	0.62 0.62	0.75 PtRu 0.75 PtRu	80 80	FAA-3-05-RF	833 615	This work
L-FeMn	lignin	0.8	0.4 PtRu	60	HDPE	261	[47]
PDCC_$ZnCl_2$	peat	4	0.67 PtRu	60	FAA-3-50	51	[80]
PBC/900/M	pig blood	3	0.4 PtRu	60	FAA-3-20	658	[81]
Zn-Fe_{SA}-PC/950	pig blood	3	0.4 PtRu	60	FAA-3-20	352	[82]
SNBC12	bamboo	2	0.5 Pt	60	FAA-3-50	217	[83]
NBSCP	bean sprout	3	0.4 Pt	60	FAA-3-50	172.2	[84]
N-F/CTC	silk cotton	2	0.5 Pt	40	FAA-3-50	13.3	[85]

Summary

The main goal of present master's thesis was to prepare non-precious metal catalysts for electrochemical oxygen reduction reaction (ORR) using lignin as a sustainable precursor. Porous carbon-based catalysts, doped with nitrogen and transition metals (Fe and Co), were prepared via a simple pyrolysis method from lignin, dicyandiamide and metal salts. Magnesium acetate was used as the template precursor, and MgO formed in high-temperature pyrolysis was dissolved in dilute acid. The iron content in the catalyst materials was varied and for comparison, a bimetallic catalyst containing Fe and Co was also prepared.

The results of scanning electron microscopy (SEM) studies showed that the materials have similar morphology consisting of irregular, sheet-like carbon structures. Transmission electron microscopy (TEM) images revealed a uniform dispersion of nitrogen element in the catalyst materials, confirming successful nitrogen doping. Transition metals were partly found to be uniformly dispersed, presumably as M-N_x centres, but also forming nanoparticles, which consisted of Fe_3C or FeCo alloy, as revealed by X-ray diffraction (XRD) analysis. The results of the N_2 physisorption analysis showed that the addition of Mg acetate increases the specific surface area and pore volume of Fe-containing catalyst materials. The energy-dispersive X-ray spectroscopy (EDX) analysis and X-ray photoelectron spectroscopy (XPS) studies were carried out to characterise the elemental content of the catalyst materials.

The electrocatalytic activity of the catalysts towards the oxygen reduction reaction was studied using the rotating disc electrode (RDE) method. The effect of iron content in catalysts on the catalyst ORR performance in alkaline solution was evaluated. A bimetallic (FeCo) catalyst was slightly less active for ORR than the most active iron-based material. The catalysts were proved to be rather stable after potential cycling for 10000 cycles. In acidic solution, the catalysts also showed a rather high electrocatalytic activity towards the ORR.

In a single-cell H_2/O_2 anion-exchange membrane fuel cell (AEMFC) tests the bimetallic catalyst performed better than iron-containing material, showing a peak power density of 675 mW cm^{-2} at 60 °C and 833 mW cm^{-2} at 80 °C.

The results show that highly active non-precious metal catalysts for oxygen reduction reaction can be prepared from lignin as a carbon source in high-temperature pyrolysis. The electrocatalytic activity of the materials depends on their transition metal content and porous structure, which can be tuned by using a magnesium-based template in the synthesis process.

Kokkuvõte

Magistritöö eesmärgiks oli valmistada mitteväärismetallkatalüsaatorid hapniku elektrokeemilise redutseerimisreaktsiooni katalüüsimiseks, kasutades lähteainena ligniini. Poorsed lämmastiku ja siirdemetallidega (Fe ja Co) dopeeritud süsinikkatalüsaatorid valmistati kõrgtemperatuursel pürolüüsil ligniinist, ditsüaandiamiidist ja metallisooladest. Materjalide poorsuse suurendamiseks lisati magneesiumatsetaati ja sellest kõrgtemperatuursel pürolüüsil moodustunud MgO matriits eemaldati lahjas happelahuses. Katalüsaatormaterjalide rauasisaldust varieeriti ja võrdluseks valmistati ka Fe ja Co sisaldav bimetalne katalüsaator.

Skaneeriva elektronmikroskoopia kujutised näitasid, et materjalid olid sarnase morfoloogiaga ning koosnesid ebakorrapärastest liistakutaolistest süsinikstruktuuridest. Läbistuselektronmikroskoopia uuringud osutasid lämmastiku ühtlasele jaotumisele katalüsaatormaterjalides, mis kinnitas dopeerimise edukust. Siirdemetallid esinesid üle materjali hajutatuna, arvatavasti M-N_x tsentritena, kuid moodustasid ka nanoosakesi, mis röntgendifraktsioonanalüüsi andmete kohaselt sisaldasid FeCo sulamit või Fe_3C. Lämmastiku sorptsioonianalüüsi tulemused näitasid, et magneesiumatsetaadi lisamine suurendab Fe-sisaldavate katalüsaatormaterjalide eripinda ja pooride ruumala. Katalüsaatormaterjalide elementsisalduse määramiseks viidi läbi energiajaotusröntgenanalüüsi ja röntgenfotoelektronspektroskoopia uuringud.

Katalüsaatorite elektrokatalüütilist aktiivsust hapniku redutseerimisel uuriti pöörleva ketaselektroodi meetodil. Leiti, et katalüsaatorite aktiivsus leeliselises lahuses sõltub nende rauasisaldusest ning bimetalne (FeCo) katalüsaator on veidi madalama aktiivsusega kui kõige aktiivsem rauapõhine materjal. Potentsiaali tsükleerimisel 10000 tsükli jooksul osutusid katalüsaatorid üsna stabiilseteks. Happelises lahuses pöörleva ketaselektroodi mõõtmistel olid katalüsaatorid hapniku redutseerumisel samuti üsna kõrge elektrokatalüütilise aktiivsusega.

Anioonvahetusmembraaniga H_2/O_2 kütuseelemendi testides saadi bimetalse katalüsaatoriga kõrgem maksimaalne võimsustihedus (P_{max}) võrreldes rauda sisaldava materjaliga, temperatuuril 60 °C P_{max} = 675 mW cm^{-2} ja temperatuuril 80 °C P_{max} = 833 mW cm^{-2}.

Tulemused näitavad, et ligniini kasutamisel süsinikuallikana on pürolüüsil võimalik valmistada väga aktiivseid mitteväärismetallkatalüsaatoreid hapniku redutseerimisreaktsiooni jaoks. Materjalide elektrokatalüütiline aktiivsus sõltub nende siirdemetallide sisaldusest ja poorsest struktuurist, mida saab mõjutada kasutades sünteesiprotsessis matriitsina magneesiumoksiidi.

References

[1] J.O. Abe, A.P.I. Popoola, E. Ajenifuja, O.M. Popoola, Hydrogen energy, economy and storage: Review and recommendation, Int. J. Hydrogen Energy 44 (2019) 15072–15086. https://doi.org/10.1016/j.ijhydene.2019.04.068.

[2] H. Nazir, N. Muthuswamy, C. Louis, S. Jose, J. Prakash, M.E.M. Buan, C. Flox, S. Chavan, X. Shi, P. Kauranen, T. Kallio, G. Maia, K. Tammeveski, N. Lymperopoulos, E. Carcadea, E. Veziroglu, A. Iranzo, A.M. Kannan, Is the H2 economy realizable in the foreseeable future? Part III: H2 usage technologies, applications, and challenges and opportunities, Int. J. Hydrogen Energy 45 (2020) 28217–28239. https://doi.org/10.1016/j.ijhydene.2020.07.256.

[3] P.C.K. Vesborg, T.F. Jaramillo, Addressing the terawatt challenge: scalability in the supply of chemical elements for renewable energy, RSC Adv. 2 (2012) 7933–7947. https://doi.org/10.1039/C2RA20839C.

[4] S.T. Thompson, D. Papageorgopoulos, Platinum group metal-free catalysts boost cost competitiveness of fuel cell vehicles, Nat. Catal. 2 (2019) 558–561. https://doi.org/10.1038/s41929-019-0291-x.

[5] B.G. Pollet, S.S. Kocha, I. Staffell, Current status of automotive fuel cells for sustainable transport, Curr. Opin. Electrochem. 16 (2019) 90–95. https://doi.org/10.1016/j.coelec.2019.04.021.

[6] R. Jasinski, A New Fuel Cell Cathode Catalyst, Nature 201 (1964) 1212–1213. https://doi.org/10.1038/2011212a0.

[7] A. Sarapuu, E. Kibena-Põldsepp, M. Borghei, K. Tammeveski, Electrocatalysis of oxygen reduction on heteroatom-doped nanocarbons and transition metal–nitrogen–carbon catalysts for alkaline membrane fuel cells, J. Mater. Chem. A 6 (2018) 776–804. https://doi.org/10.1039/C7TA08690C.

[8] J. Quílez-Bermejo, E. Morallón, D. Cazorla-Amorós, Metal-free heteroatom-doped carbon-based catalysts for ORR: A critical assessment about the role of heteroatoms, Carbon 165 (2020) 434–454. https://doi.org/10.1016/j.carbon.2020.04.068.

[9] P. Kaur, G. Verma, S.S. Sekhon, Biomass derived hierarchical porous carbon materials as oxygen reduction reaction electrocatalysts in fuel cells. Prog. Mater. Sci. 102 (2019) 1–71. https://doi.org/10.1016/j.pmatsci.2018.12.002.

[10] J.S. Bates, M.R. Johnson, F. Khamespanah, T.W. Root, S.S. Stahl, Heterogeneous M-N-C Catalysts for Aerobic Oxidation Reactions: Lessons from Oxygen Reduction Electrocatalysts, Chem. Rev. 123 (2023) 6233–6256. https://doi.org/10.1021/acs.chemrev.2c00424.

[11] I. Kruusenberg, J. Leis, M. Arulepp, K. Tammeveski, Oxygen reduction on carbon nanomaterial-modified glassy carbon electrodes in alkaline solution, J. Solid State Electrochem. 14 (2010) 1269–1277. https://doi.org/10.1007/s10008-009-0930-2.

[12] J. Lilloja, E. Kibena-Põldsepp, M. Merisalu, P. Rauwel, L. Matisen, A. Niilisk, E.S.F. Cardoso, G. Maia, V. Sammelselg, K. Tammeveski, An Oxygen Reduction Study of Graphene-Based Nanomaterials of Different Origin, Catalysts 6 (2016) 108. https://doi.org/10.3390/catal6070108.

[13] R. Jäger, P.E. Kasatkin, E. Härk, E. Lust, Oxygen reduction on molybdenum carbide derived micromesoporous carbon electrode in alkaline solution, Electrochem. Commun. 35 (2013) 97–99. https://doi.org/10.1016/j.elecom.2013.08.001.

[14] K. Gong, F. Du, Z. Xia, M. Durstock, L. Dai, Nitrogen-doped carbon nanotube arrays with high electrocatalytic activity for oxygen reduction, Science 323 (2009) 760–764. https://doi.org/10.1126/science.1168049.

[15] A. Dessalle, J. Quílez-Bermejo, V. Fierro, F. Xu, A. Celzard, Recent progress in the development of efficient biomass-based ORR electrocatalysts, Carbon 203 (2023) 237–260. https://doi.org/10.1016/j.carbon.2022.11.073.
[16] A. Shetty, V. Molahalli, A. Sharma, G. Hegde, Biomass-Derived Carbon Materials in Heterogeneous Catalysis: A Step towards Sustainable Future, Catalysts 13 (2023) 20. https://doi.org/10.3390/catal13010020.
[17] R. Li, Z. Wei, X. Gou, W. Xu, Phosphorus-doped graphene nanosheets as efficient metal-free oxygen reduction electrocatalysts, RSC Adv. 3 (2013) 9978–9984. https://doi.org/10.1039/C3RA41079J.
[18] Z.-H. Sheng, H.-L. Gao, W.-J. Bao, F.-B. Wang, X.-H. Xia, Synthesis of boron doped graphene for oxygen reduction reaction in fuel cells, J. Mater. Chem. 22 (2011) 390–395. https://doi.org/10.1039/C1JM14694G.
[19] X. Sun, Y. Zhang, P. Song, J. Pan, L. Zhuang, W. Xu, W. Xing, Fluorine-Doped Carbon Blacks: Highly Efficient Metal-Free Electrocatalysts for Oxygen Reduction Reaction, ACS Catal. 3 (2013) 1726–1729. https://doi.org/10.1021/cs400374k.
[20] Z. Yao, H. Nie, Z. Yang, X. Zhou, Z. Liu, S. Huang, Catalyst-free synthesis of iodine-doped graphenevia a facile thermal annealing process and its use for electrocatalytic oxygen reduction in an alkaline medium, Chem. Commun. 48 (2012) 1027–1029. https://doi.org/10.1039/C2CC16192C.
[21] L. Yang, J. Shui, L. Du, Y. Shao, J. Liu, L. Dai, Z. Hu, Carbon-Based Metal-Free ORR Electrocatalysts for Fuel Cells: Past, Present, and Future, Adv. Mater. 31 (2019) e1804799. https://doi.org/10.1002/adma.201804799.
[22] H. Wang, T. Maiyalagan, X. Wang, Review on Recent Progress in Nitrogen-Doped Graphene: Synthesis, Characterization, and Its Potential Applications, ACS Catal. 2 (2012) 781–794. https://doi.org/10.1021/cs200652y.
[23] C.V. Rao, C.R. Cabrera, Y. Ishikawa, In Search of the Active Site in Nitrogen-Doped Carbon Nanotube Electrodes for the Oxygen Reduction Reaction, J. Phys. Chem. Lett. 1 (2010) 2622–2627. https://doi.org/10.1021/jz100971v.
[24] H. Miao, S. Li, Z. Wang, S. Sun, M. Kuang, Z. Liu, J. Yuan, Enhancing the pyridinic N content of Nitrogen-doped graphene and improving its catalytic activity for oxygen reduction reaction, Int. J. Hydrogen Energy 42 (2017) 28298–28308. https://doi.org/10.1016/j.ijhydene.2017.09.138.
[25] K. Kisand, A. Sarapuu, J.C. Douglin, A. Kikas, A. Treshchalov, M. Käärik, H.-M. Piirsoo, P. Paiste, J. Aruväli, J. Leis, V. Kisand, A. Tamm, D.R. Dekel, K. Tammeveski, Templated Nitrogen-, Iron-, and Cobalt-Doped Mesoporous Nanocarbon Derived from an Alkylresorcinol Mixture for Anion-Exchange Membrane Fuel Cell Application, ACS Catal. 12 (2022) 14050–14061. https://doi.org/10.1021/acscatal.2c03683.
[26] T. Murata, K. Kotsuki, H. Murayama, R. Tsuji, Y. Morita, Metal-free electrocatalysts for oxygen reduction reaction based on trioxotriangulene, Commun. Chem. 2 (2019) 1–8. https://doi.org/10.1038/s42004-019-0149-9.
[27] G. Wu, A. Santandreu, W. Kellogg, S. Gupta, O. Ogoke, H. Zhang, H.-L. Wang, L. Dai, Carbon nanocomposite catalysts for oxygen reduction and evolution reactions: From nitrogen doping to transition-metal addition, Nano Energy 29 (2016) 83–110. https://doi.org/10.1016/j.nanoen.2015.12.032.
[28] N. Ramaswamy, U. Tylus, Q. Jia, S. Mukerjee, Activity Descriptor Identification for Oxygen Reduction on Nonprecious Electrocatalysts: Linking Surface Science to Coordination Chemistry, J. Am. Chem. Soc. 135 (2013) 15443–15449. https://doi.org/10.1021/ja405149m.
[29] R. Praats, M. Käärik, A. Kikas, V. Kisand, J. Aruväli, P. Paiste, M. Merisalu, A. Sarapuu, J. Leis, V. Sammelselg, J.C. Douglin, D.R. Dekel, K. Tammeveski, Electroreduction of

oxygen on cobalt phthalocyanine-modified carbide-derived carbon/carbon nanotube composite catalysts, J. Solid State Electrochem. 25 (2021) 57–71. https://doi.org/10.1007/s10008-020-04543-z.
[30] K. Li, Y. Li, W. Peng, G. Zhang, F. Zhang, X. Fan, Bimetallic Iron–Cobalt Catalysts and Their Applications in Energy-Related Electrochemical Reactions, Catalysts 9 (2019) 762. https://doi.org/10.3390/catal9090762.
[31] J. Wang, H. Zhong, L.A. Estudillo-Wong, H. Li, N. Alonso-Vante, D. Li, P. Tang, Y. Feng, Synthesis and electrocatalytic performance of N-doped graphene embedded with Co/CoO nanoparticles towards oxygen evolution and reduction reactions, Catal. Commun. 164 (2022) 106428. https://doi.org/10.1016/j.catcom.2022.106428.
[32] L. Chen, Y. Zhang, L. Dong, W. Yang, X. Liu, L. Long, C. Liu, S. Dong, J. Jia, Synergistic effect between atomically dispersed Fe and Co metal sites for enhanced oxygen reduction reaction, J. Mater. Chem. A 8 (2020) 4369–4375. https://doi.org/10.1039/C9TA12516G.
[33] H. Tan, J. Tang, J. Kim, Y.V. Kaneti, Y.-M. Kang, Y. Sugahara, Y. Yamauchi, Rational design and construction of nanoporous iron- and nitrogen-doped carbon electrocatalysts for oxygen reduction reaction, J. Mater. Chem. A 7 (2019) 1380–1393. https://doi.org/10.1039/C8TA08870E.
[34] Z. Hao, Y. Ma, Y. Chen, P. Fu, P. Wang, Non-Noble Metal Catalysts in Cathodic Oxygen Reduction Reaction of Proton Exchange Membrane Fuel Cells: Recent Advances, Nanomaterials (Basel) 12 (2022) 3331. https://doi.org/10.3390/nano12193331.
[35] C.-W. Ye, L. Xu, Recent advances in the design of a high performance metal–nitrogen–carbon catalyst for the oxygen reduction reaction, J. Mater. Chem. A 9 (2021) 22218–22247. https://doi.org/10.1039/D1TA05605K.
[36] L. Du, G. Zhang, X. Liu, A. Hassanpour, M. Dubois, A.C. Tavares, S. Sun, Biomass-derived nonprecious metal catalysts for oxygen reduction reaction: The demand-oriented engineering of active sites and structures, Carbon Energy 2 (2020) 561–581. https://doi.org/10.1002/cey2.73.
[37] M. Borghei, J. Lehtonen, L. Liu, O.J. Rojas, Advanced Biomass-Derived Electrocatalysts for the Oxygen Reduction Reaction, Adv. Mater. 30 (2018) 1703691. https://doi.org/10.1002/adma.201703691.
[38] M. Graglia, J. Pampel, T. Hantke, T.-P. Fellinger, D. Esposito, Nitro Lignin-Derived Nitrogen-Doped Carbon as an Efficient and Sustainable Electrocatalyst for Oxygen Reduction, ACS Nano 10 (2016) 4364–4371. https://doi.org/10.1021/acsnano.5b08040.
[39] R. Jia, C. He, Q. Li, S.-Y. Liu, G. Liao, Renewable plant-derived lignin for electrochemical energy systems, Trends Biotechnol. 40 (2022) 1425–1438. https://doi.org/10.1016/j.tibtech.2022.07.017.
[40] B. Szczęśniak, J. Phuriragpitikhon, J. Choma, M. Jaroniec, Recent advances in the development and applications of biomass-derived carbons with uniform porosity, J. Mater. Chem. A 8 (2020) 18464–18491. https://doi.org/10.1039/D0TA05094F.
[41] S. Das, S. Ghosh, T. Kuila, N.C. Murmu, A. Kundu, Biomass-Derived Advanced Carbon-Based Electrocatalysts for Oxygen Reduction Reaction, Biomass 2 (2022) 155–177. https://doi.org/10.3390/biomass2030010.
[42] M. Inagaki, S. Kobayashi, F. Kojin, N. Tanaka, T. Morishita, B. Tryba, Pore structure of carbons coated on ceramic particles, Carbon 42 (2004) 3153–3158. https://doi.org/10.1016/j.carbon.2004.07.029.
[43] K. Kisand, A. Sarapuu, A. Kikas, V. Kisand, M. Rähn, A. Treshchalov, M. Käärik, H.-M. Piirsoo, J. Aruväli, P. Paiste, J. Leis, V. Sammelselg, A. Tamm, K. Tammeveski, Bifunctional multi-metallic nitrogen-doped nanocarbon catalysts derived from 5-methylresorcinol, Electrochem. Commun. 124 (2021) 106932. https://doi.org/10.1016/j.elecom.2021.106932.

[44] M. Zhang, Y. Song, H. Tao, C. Yan, J. Masa, Y. Liu, X. Shi, S. Liu, X. Zhang, Z. Sun, Lignosulfonate biomass derived N and S co-doped porous carbon for efficient oxygen reduction reaction, Sustain. Energy Fuels 2 (2018) 1820–1827. https://doi.org/10.1039/C8SE00231B.
[45] D. Yan, Y. Han, Z. Ma, Q. Wang, X. Wang, Y. Li, G. Sun, Magnesium lignosulfonate-derived N, S co-doped 3D flower-like hierarchically porous carbon as an advanced metal-free electrocatalyst towards oxygen reduction reaction, Int. J. Biol. Macromol. 209 (2022) 904–911. https://doi.org/10.1016/j.ijbiomac.2022.04.063.
[46] Z. Ma, Y. Han, X. Wang, G. Sun, Y. Li, Lignin-derived hierarchical porous flower-like carbon nanosheets decorated with biomass carbon quantum dots for efficient oxygen reduction, Colloids Surf. A: 652 (2022) 129818. https://doi.org/10.1016/j.colsurfa.2022.129818.
[47] M. Muhyuddin, A. Friedman, F. Poli, E. Petri, H. Honig, F. Basile, A. Fasolini, R. Lorenzi, E. Berretti, M. Bellini, A. Lavacchi, L. Elbaz, C. Santoro, F. Soavi, Lignin-derived bimetallic platinum group metal-free oxygen reduction reaction electrocatalysts for acid and alkaline fuel cells, J. Power Sources 556 (2023) 232416. https://doi.org/10.1016/j.jpowsour.2022.232416.
[48] B. Huang, J. Jiang, N-doped carbon nanosheets derived from lignin as a novel bifunctional electrocatalyst for rechargeable zinc-air battery, Diamond Relat. Mater. 128 (2022) 109291. https://doi.org/10.1016/j.diamond.2022.109291.
[49] C. Li, Y. Wu, M. Fu, X. Zhao, S. Zhai, Y. Yan, L. Zhang, X. Zhang, Preparation of Fe/N Double Doped Carbon Nanotubes from Lignin in Pennisetum as Oxygen Reduction Reaction Electrocatalysts for Zinc–Air Batteries, ACS Appl. Energy Mater. 5 (2022) 4340–4350. https://doi.org/10.1021/acsaem.1c03956.
[50] R. Dong, Z. Yang, Y. Fu, Z. Chen, Y. Hu, Y. Zhou, H. Qin, Aminated lignin chelated metal derived bifunctional electrocatalyst with high catalytic performance, Appl. Surf. Sci. 580 (2022) 152205. https://doi.org/10.1016/j.apsusc.2021.152205.
[51] B.G. Pollet, I. Staffell, J.L. Shang, Current status of hybrid, battery and fuel cell electric vehicles: From electrochemistry to market prospects, Electrochim. Acta 84 (2012) 235–249. https://doi.org/10.1016/j.electacta.2012.03.172.
[52] D.R. Dekel, Review of cell performance in anion exchange membrane fuel cells, J. Power Sources 375 (2018) 158–169. https://doi.org/10.1016/j.jpowsour.2017.07.117.
[53] E.B. Agyekum, J.D. Ampah, T. Wilberforce, S. Afrane, C. Nutakor, Research Progress, Trends, and Current State of Development on PEMFC-New Insights from a Bibliometric Analysis and Characteristics of Two Decades of Research Output, Membranes 12 (2022) 1103. https://doi.org/10.3390/membranes12111103.
[54] Md.M. Hossen, Md.S. Hasan, Md.R.I. Sardar, J. bin Haider, Mottakin, K. Tammeveski, P. Atanassov, State-of-the-art and developmental trends in platinum group metal-free cathode catalyst for anion exchange membrane fuel cell (AEMFC), Appl. Catal. B: Environ. 325 (2023) 121733. https://doi.org/10.1016/j.apcatb.2022.121733.
[55] M. Hren, M. Božič, D. Fakin, K.S. Kleinschek, S. Gorgieva, Alkaline membrane fuel cells: anion exchange membranes and fuels, Sustainable Energy Fuels 5 (2021) 604–637. https://doi.org/10.1039/D0SE01373K.
[56] W.E. Mustain, Understanding how high-performance anion exchange membrane fuel cells were achieved: Component, interfacial, and cell-level factors, Curr. Opin. Electrochem. 12 (2018) 233–239. https://doi.org/10.1016/j.coelec.2018.11.010.
[57] M. Mamlouk, J.A. Horsfall, C. Williams, K. Scott, Radiation grafted membranes for superior anion exchange polymer membrane fuel cells performance, Int. J. Hydrogen Energy 37 (2012) 11912–11920. https://doi.org/10.1016/j.ijhydene.2012.05.117.

[58] W.E. Mustain, M. Chatenet, M. Page, Y.S. Kim, Durability challenges of anion exchange membrane fuel cells, Energy Environ. Sci. 13 (2020) 2805–2838. https://doi.org/10.1039/D0EE01133A.
[59] T.B. Ferriday, P.H. Middleton, Alkaline fuel cell technology - A review, Int. J. Hydrogen Energy 46 (2021) 18489–18510. https://doi.org/10.1016/j.ijhydene.2021.02.203.
[60] G. Das, J.-H. Choi, P.K.T. Nguyen, D.-J. Kim, Y.S. Yoon, Anion Exchange Membranes for Fuel Cell Application: A Review, Polymers 14 (2022) 1197. https://doi.org/10.3390/polym14061197.
[61] S.T. Thompson, D. Peterson, D. Ho, D. Papageorgopoulos, Perspective—The Next Decade of AEMFCs: Near-Term Targets to Accelerate Applied R&D, J. Electrochem. Soc. 167 (2020) 084514. https://doi.org/10.1149/1945-7111/ab8c88.
[62] A.J. Bard, L.R. Faulkner, Electrochemical Methods, 2nd ed., Wiley, New York, 2001.
[63] R.E. Davis, G.L. Horvath, C.W. Tobias, The solubility and diffusion coefficient of oxygen in potassium hydroxide solutions, Electrochim. Acta 12 (1967) 287–297. https://doi.org/10.1016/0013-4686(67)80007-0.
[64] S. Gottesfeld, I.D. Raistrick, S. Srinivasan, Oxygen Reduction Kinetics on a Platinum RDE Coated with a Recast Nafion Film, J. Electrochem. Soc. 134 (1987) 1455. https://doi.org/10.1149/1.2100689.
[65] J. Lilloja, E. Kibena-Põldsepp, A. Sarapuu, J.C. Douglin, M. Käärik, J. Kozlova, P. Paiste, A. Kikas, J. Aruväli, J. Leis, V. Sammelselg, D.R. Dekel, K. Tammeveski, Transition-Metal- and Nitrogen-Doped Carbide-Derived Carbon/Carbon Nanotube Composites as Cathode Catalysts for Anion-Exchange Membrane Fuel Cells, ACS Catal. 11 (2021) 1920–1931. https://doi.org/10.1021/acscatal.0c03511.
[66] N. Zion, J.C. Douglin, D.A. Cullen, P. Zelenay, D.R. Dekel, L. Elbaz, Porphyrin Aerogel Catalysts for Oxygen Reduction Reaction in Anion-Exchange Membrane Fuel Cells, Adv. Funct. Mater. 31 (2021) 2100963. https://doi.org/10.1002/adfm.202100963.
[67] Y. Kumar, E. Kibena-Põldsepp, J. Kozlova, M. Rähn, A. Treshchalov, A. Kikas, V. Kisand, J. Aruväli, A. Tamm, J.C. Douglin, S.J. Folkman, I. Gelmetti, F.A. Garcés-Pineda, J.R. Galán-Mascarós, D.R. Dekel, K. Tammeveski, Bifunctional Oxygen Electrocatalysis on Mixed Metal Phthalocyanine-Modified Carbon Nanotubes Prepared via Pyrolysis, ACS Appl. Mater. Interfaces 13 (2021) 41507–41516. https://doi.org/10.1021/acsami.1c06737.
[68] J.C. Douglin, R.K. Singh, S. Haj-Bsoul, S. Li, J. Biemolt, N. Yan, J.R. Varcoe, G. Rothenberg, D.R. Dekel, A high-temperature anion-exchange membrane fuel cell with a critical raw material-free cathode, Chem. Eng. J. Adv. 8 (2021) 100153. https://doi.org/10.1016/j.ceja.2021.100153.
[69] C. Hu, Y. Zhou, R. Ma, Q. Liu, J. Wang, Reactive template synthesis of nitrogen-doped graphene-like carbon nanosheets derived from hydroxypropyl methylcellulose and dicyandiamide as efficient oxygen reduction electrocatalysts, J. Power Sources 345 (2017) 120–130. https://doi.org/10.1016/j.jpowsour.2017.01.124.
[70] Q. Li, D. Xu, X. Ou, F. Yan, Nitrogen-Doped Graphitic Porous Carbon Nanosheets Derived from In Situ Formed g-C3N4 Templates for the Oxygen Reduction Reaction, Asian J. Chem. 12 (2017) 1816–1823. https://doi.org/10.1002/asia.201700586.
[71] I. Childres, L.A. Jauregui, J. Tian, Y.P. Chen, Effect of oxygen plasma etching on graphene studied using Raman spectroscopy and electronic transport measurements, New J. Phys. 13 (2011) 025008. https://doi.org/10.1088/1367-2630/13/2/025008.
[72] A. Gomez-Martin, Z. Schnepp, J. Ramirez-Rico, Structural Evolution in Iron-Catalyzed Graphitization of Hard Carbons, Chem. Mater. 33 (2021) 3087–3097. https://doi.org/10.1021/acs.chemmater.0c04385.

[73] K. Artyushkova, A. Serov, S. Rojas-Carbonell, P. Atanassov, Chemistry of Multitudinous Active Sites for Oxygen Reduction Reaction in Transition Metal–Nitrogen–Carbon Electrocatalysts, J. Phys. Chem. C 119 (2015) 25917–25928. https://doi.org/10.1021/acs.jpcc.5b07653.
[74] M.C. Biesinger, B.P. Payne, A.P. Grosvenor, L.W.M. Lau, A.R. Gerson, R.St.C. Smart, Resolving surface chemical states in XPS analysis of first row transition metals, oxides and hydroxides: Cr, Mn, Fe, Co and Ni, Appl. Surf. Sci. 257 (2011) 2717–2730. https://doi.org/10.1016/j.apsusc.2010.10.051.
[75] I. Bertóti, M. Mohai, K. László, Surface modification of graphene and graphite by nitrogen plasma: Determination of chemical state alterations and assignments by quantitative X-ray photoelectron spectroscopy, Carbon 84 (2015) 185–196. https://doi.org/10.1016/j.carbon.2014.11.056.
[76] P.G. Santori, F.D. Speck, S. Cherevko, H.A. Firouzjaie, X. Peng, W.E. Mustain, F. Jaouen, High Performance FeNC and Mn-oxide/FeNC Layers for AEMFC Cathodes, J. Electrochem. Soc. 167 (2020) 134505. https://doi.org/10.1149/1945-7111/abb7e0.
[77] J. Lilloja, E. Kibena-Põldsepp, A. Sarapuu, M. Käärik, J. Kozlova, P. Paiste, A. Kikas, A. Treshchalov, J. Leis, A. Tamm, V. Kisand, S. Holdcroft, K. Tammeveski, Transition metal and nitrogen-doped mesoporous carbons as cathode catalysts for anion-exchange membrane fuel cells, Appl. Catal. B: Environ. 306 (2022) 121113. https://doi.org/10.1016/j.apcatb.2022.121113.
[78] I. Matanovic, K. Artyushkova, P. Atanassov, Understanding PGM-free catalysts by linking density functional theory calculations and structural analysis: Perspectives and challenges, Curr. Opin. Electrochem. 9 (2018) 137–144. https://doi.org/10.1016/j.coelec.2018.03.009.
[79] Y. Yang, C.R. Peltier, R. Zeng, R. Schimmenti, Q.H. Li, X. Huang, Z.F. Yan, G. Potsi, R. Selhorst, X.Y. Lu, W.X. Xu, M. Tader, A.V. Soudackov, H.G. Zhang, M. Krumov, E. Murray, P.T. Xu, J. Hitt, L.X. Xu, H.Y. Ko, B.G. Ernst, C. Bundschu, A. Luo, D. Markovich, M.X. Hu, C. He, H.S. Wang, J.Y. Fang, R.A. DiStasio, L.F. Kourkoutis, A. Singer, K.J.T. Noonan, L. Xiao, L. Zhuang, B.S. Pivovar, P. Zelenay, E. Herrero, J.M. Feliu, J. Suntivich, E.P. Giannelis, S. Hammes-Schiffer, T. Arias, M. Mavrikakis, T.E. Mallouk, J.D. Brock, D.A. Muller, F.J. DiSalvo, G.W. Coates, H.D. Abruna, Electrocatalysis in Alkaline Media and Alkaline Membrane-Based Energy Technologies, Chem. Rev. 122 (2022) 6117-6321. https://doi.org/10.1021/acs.chemrev.1c00331
[80] P. Teppor, R. Jäger, M. Paalo, A. Adamson, M. Härmas, O. Volobujeva, J. Aruväli, R. Palm, E. Lust, Peat as a carbon source for non-platinum group metal oxygen electrocatalysts and AEMFC cathodes, Int. J. Hydrogen Energy 47 (2022) 16908–16920. https://doi.org/10.1016/j.ijhydene.2022.03.199.
[81] J. Lee, H.S. Kim, J.-H. Jang, E.-H. Lee, H.-W. Jeong, K.-S. Lee, P. Kim, S.J. Yoo, Atomic-Scale Engineered Fe Single-Atom Electrocatalyst Based on Waste Pig Blood for High-Performance AEMFCs, ACS Sustainable Chem. Eng. 9 (2021) 7863–7872. https://doi.org/10.1021/acssuschemeng.1c01590.
[82] H.S. Kim, J. Lee, J.-H. Jang, H. Jin, V.K. Paidi, S.-H. Lee, K.-S. Lee, P. Kim, S.J. Yoo, Waste pig blood-derived 2D Fe single-atom porous carbon as an efficient electrocatalyst for zinc–air batteries and AEMFCs, Appl. Surf. Sci. 563 (2021) 150208. https://doi.org/10.1016/j.apsusc.2021.150208.
[83] M.-J. Kim, J.E. Park, S. Kim, M.S. Lim, A. Jin, O.-H. Kim, M.J. Kim, K.-S. Lee, J. Kim, S.-S. Kim, Y.-H. Cho, Y.-E. Sung, Biomass-Derived Air Cathode Materials: Pore-Controlled S,N-Co-doped Carbon for Fuel Cells and Metal–Air Batteries, ACS Catal. 9 (2019) 3389–3398. https://doi.org/10.1021/acscatal.8b03730.

[84] D.W. Lee, J.-H. Jang, I. Jang, Y.S. Kang, S. Jang, K.Y. Lee, J.H. Jang, H.-J. Kim, S.J. Yoo, Bio-Derived Co2P Nanoparticles Supported on Nitrogen-Doped Carbon as Promising Oxygen Reduction Reaction Electrocatalyst for Anion Exchange Membrane Fuel Cells, Small. 15 (2019) 1902090. https://doi.org/10.1002/smll.201902090.
[85] S. Akula, B. Balasubramaniam, P. Varathan, A.K. Sahu, Nitrogen–Fluorine Dual Doped Porous Carbon Derived from Silk Cotton as Efficient Oxygen Reduction Catalyst for Polymer Electrolyte Fuel Cells, ACS Appl. Energy Mater. 2 (2019) 3253–3263. https://doi.org/10.1021/acsaem.9b00100.

Acknowledgements

I would like to express my sincere gratitude to my supervisors, Dr. Ave Sarapuu and Professor Kaido Tammeveski, for their essential assistance, scientific direction, and moral support throughout the years.

I want to express my profound gratitude to everyone in our working group who has offered me guidance, motivation, or just nice words and words of support. I would especially like to thank Dr. Jaana Lilloja for always supporting me during my research years.

I want to express my gratitude to the co-authors of the works on which this thesis is based: Dr. Jekaterina Kozlova, Dr. Maike Käärik, Dr. Alexey Treshchalov, Jaan Aruväli, Dr. Arvo Kikas, John C. Douglin and Professor Dario R. Dekel.

I also want to express my gratitude to my family and friends for their encouragement support and prayers. My Husband Muhammad Bilal Rasheed deserves a special thank you for all of his efforts and support during my studies and the years leading up to them. My friend Dr. Iram Tufail who helped me throughout my studies in University of Tartu.

This work was financially supported by Estonian Research Council (grant PRG723).

Appendix

Non-exclusive licence to reproduce the thesis and make the thesis public

I, Umber Sajjad,

1. grant the University of Tartu a free permit (non-exclusive licence) to:
   reproduce, for the purpose of preservation, including for adding to the DSpace digital archives until the expiry of the term of copyright, my thesis

'Oxygen electroreduction on lignin-derived non-precious metal catalysts', supervised by Prof. Kaido Tammeveski and Dr. Ave Sarapuu.

2. I grant the University of Tartu the permit to make the thesis specified in point 1 available to the public via the web environment of the University of Tartu, including via the Dspace digital archives, under the Creative Commons licence CC BY NC ND 4.0, which allows, by giving appropriate credit to the author, to reproduce, distribute the work and communicate it to the public, and prohibits the creation of derivative works and any commercial use of the work from **05/06/2026** until the expiry of the term of copyright,
3. I am aware that the author retains the rights specified in points 1 and 2.
4. I confirm that granting the non-exclusive licence does not infringe other persons' intellectual property rights or rights arising from the personal data protection legislation.

Umber Sajjad

29/05/2023